

Improvements to stellar structure models, based on a grid of 3D convection simulations. II. Calibrating the mixing-length formulation

Regner Trampedach^{1,2*}, Robert F. Stein³, Jørgen Christensen-Dalsgaard¹, Åke Nordlund⁴ and Martin Asplund⁵

¹*Stellar Astrophysics Centre, Department of Physics and Astronomy, Ny Munkegade 120, Aarhus University, DK-8000 Aarhus C, Denmark*

²*JILA, University of Colorado and National Institute of Standards and Technology, 440 UCB, Boulder, CO 80309, USA*

³*Department of Physics and Astronomy, Michigan State University East Lansing, MI 48824, USA*

⁴*Astronomical Observatory/Niels Bohr Institute, Juliane Maries Vej 30, DK-2100 Copenhagen Ø, Denmark*

⁵*Research School of Astronomy and Astrophysics, Mt. Stromlo Observatory, Cotter Road, Weston ACT 2611, Australia*

Received 8 November 2021/ Accepted 8 November 2021

ABSTRACT

We perform a calibration of the mixing length of convection in stellar structure models against realistic 3D radiation-coupled hydrodynamics (RHD) simulations of convection in stellar surface layers, determining the adiabat deep in convective stellar envelopes.

The mixing-length parameter α is calibrated by matching averages of the 3D simulations to 1D stellar envelope models, ensuring identical atomic physics in the two cases. This is done for a previously published grid of solar-metallicity convection simulations, covering from 4 200 K to 6 900 K on the main sequence, and 4 300–5 000 K for giants with $\log g = 2.2$.

Our calibration results in an α varying from 1.6 for the warmest dwarf, which is just cool enough to admit a convective envelope, and up to 2.05 for the coolest dwarfs in our grid. In between these is a triangular plateau of $\alpha \sim 1.76$. The Sun is located on this plateau and has seen little change during its evolution so far. When stars ascend the giant branch, they largely do so along tracks of constant α , with α decreasing with increasing mass.

Key words: Stars: atmospheres – stars: evolution – convection

1 INTRODUCTION

Due to the lack of a better theory of convection in stars, the mixing-length theory (Böhm-Vitense 1958, MLT) has been in use for more than half a century. By far the largest part of the solar convection zone is very close to adiabatic, and the stratification in the bulk of the convection zone is therefore determined by the adiabatic gradient, $\nabla_{\text{ad}} = (\partial \ln T / \partial \ln p)_{\text{ad}}$, of temperature, T , and pressure, p . Convection is so efficient that the actual gradient, ∇ , need only be slightly larger than the adiabatic one, to transport the entire energy flux. In most of the convection zone the super-adiabatic gradient, $\nabla_s = \nabla - \nabla_{\text{ad}}$, is small enough, $\nabla_s \lesssim 10^{-5}$, to have no effect on the structure of the star. We therefore have no need for a theory

of convection here, except as a means to determine the adiabat of the convection zone.

This picture changes dramatically near the boundaries, especially near the upper boundary of a convective envelope. Here convection becomes exceedingly inefficient in transporting the energy flux, as radiative energy transport takes over. For the Sun, this layer of appreciable superadiabaticity only occurs in the outermost ~ 1 Mm, just below the photosphere—the region where the gas becomes optically transparent and radiation escapes. This layer, however thin, is crucial for the star as a whole, as it is the star’s insulation against the cold of space. In other words, this layer constitutes the outer boundary condition for stellar models. It is the interaction between convection and radiative transfer in this layer that sets up the entropy jump at the top of the convection zone, and hence determines the adiabat of the convection zone. Modelling stellar atmospheres is complicated and compu-

* E-mail: trampedach@lcd.colorado.edu

tationally expensive and beyond the scope of normal stellar structure calculations. Instead, the structure modeller adopts results from atmosphere models that describe the radiative transfer through the atmosphere, and, in particular, the photospheric transition from optically thick to optically thin. One solution that we also adopt is to describe this transition by the behaviour of temperature, T , with optical depth, τ , known as a $T(\tau)$ relation (e.g. Henyey, Vardya & Bodenheimer 1965). With the radiative components fixed, the adiabat is then determined by the parameters of the MLT formulation.

Hotter, late A-type stars, close to the line in the HR diagram where stars lose their convective envelopes, have such shallow convective envelopes that they do not reach an adiabat. There, convection is inefficient and transports only a minor fraction of the flux, while the temperature fluctuations and the turbulent pressure are appreciable even at the bottom of the convection zone. This is the prediction of any realistic formulation of convection, and is confirmed by convection simulations (Freytag, Ludwig & Steffen 1996; Kupka, Ballot & Muthsam 2009; Freytag & Steffen 2005; Trampedach 2005). At the other end of the spectrum we find the cool M dwarfs that are fully convective. Giants, on the other hand, are dominated by extensive convective envelopes, and strongly condensed cores. This spans the range of stars for which the present work applies.

With the advances in atomic physics as applied to astrophysics, i.e., the equation of state (EOS, e.g., Hummer & Mihalas 1988; Saumon, Chabrier & Horn 1995; Nayfonov et al. 1999; Gong, Däppen & Zejda 2001; Rogers & Nayfonov 2002; Militzer & Hubbard 2013) and opacities (Kurucz 1992b; Rogers & Iglesias 1992; Alexander & Ferguson 1994; Seaton 1995; Iglesias & Rogers 1996; Badnell et al. 2005; Ferguson et al. 2007), by far the most uncertain aspects of stellar models are associated with dynamical phenomena: semi-convection, rotational mixing, mixing by g modes, convective overshooting and the most prominent: convection itself. Phenomena that all involve turbulence, non-locality and non-linearity, which make them less amenable to analytical formulations.

The present paper is part of an effort to improve on stellar structure models, by using results from a grid of realistic 3D hydrodynamical simulations of stellar surface convection in late-type stars. This grid of simulations is presented in more detail by Trampedach et al. (2013). The first paper in this series deals with the radiative part of the stellar surface problem and presents $T(\tau)$ relations derived from the simulations (Trampedach et al. 2014, Paper I). The present paper is Paper II. Paper III will address the consequences, of the results from the first two papers, for stellar evolution (Trampedach et al. in preparation).

In Sect. 2 we outline some concepts of realistic 3D stellar surface convection and contrast with the simple local mixing-length picture, which nonetheless has some justification. In Sect. 3 we introduce the 3D convection simulations and in Sect. 4, the 1D envelope models. Our calibration of the MLT mixing length, α , by matching 1D models to the deep part of our 3D simulations is described in Sect. 5. Results of the calibration are discussed in Sect. 6, including a note on gravity darkening.

The sensitivities of 1D structure models to the physics of the outer boundary is explored in Sect. 7, which also explains the expansion of convective envelopes with increasing convective efficiency. A more detailed discussion of our solar calibration is carried out in Sect. 8, also including a perspective on semi-empirical calibrations for other stars from the literature.

We conclude in Sect. 9 where we also provide instructions for accessing our results on-line, and for using them in stellar structure codes.

This paper is not a justification of the MLT, nor is it aimed at describing the structure of the surface layers of stars. Rather, we provide a way to use MLT and a non-constant α to determine the correct adiabat of the deep convection zone, which in turn determines the depth of the convective envelope. MLT in general, and our calibration of α in particular, has limited relevance to stellar atmosphere calculations.

The present paper supersedes the work presented in Trampedach et al. (1997). The α calibration by Ludwig, Freytag & Steffen (1999, from here on LFS), against 2D simulations with grey radiative transfer, was based on a method independent of ours. Their results are similar to ours in many respects, as discussed in Sect. 6.

Asida (2000) performed a calibration against a 2D simulation of a 36° wedge of a spherical shell of a $1.2 M_\odot$ red giant, reaching below the bottom of its convective envelope. It was truncated at the top, to justify treating radiation in the diffusion approximation, and it was further assumed that $\tau = 2/3$ at the top boundary, and that the atmosphere is grey so that T_{eff} is the local temperature there. This would seem a limitation of the method, as convective efficiency is governed by radiative cooling in the photosphere. A value of $\alpha = 1.4$ is found from a sign change in the initial flux transient, as function of α of the 1D MLT models that provide the initial conditions. This seems to ignore the possibility of the interior adjusting differently from the atmosphere and the former taking place on a much longer time-scale.

Tanner, Basu & Pierre (2014) evaluated the radius- α (or equivalently mass- α) relation for MLT stellar evolution models, restricted to have a prescribed set of atmospheric parameters, T_{eff} and $\log g$. An age- α relation also results from this and they also found the metallicity dependency of these relations. They do not, however, employ results of their 3D simulations of convection, treating radiation in the Eddington approximation.

2 MIXING LENGTH VERSUS 3D CONVECTION

Comparisons between local mixing-length versions of convection and the results of 3D simulations of the hydro-, thermo- and radiation-dynamics of convection have been presented before (Chan & Sofia 1987; Stein & Nordlund 1989; Freytag, Ludwig & Steffen 1996; Nordlund & Stein 1997; Abbet et al. 1997; Nordlund & Stein 2000; Trampedach 2010; Trampedach & Stein 2011), but we would like to point out some features that are pertinent to the present calibration of the MLT mixing length.

The conventional interpretation of the mixing-length

formulation of convection is that of bubbles, eddies or convective elements that are warmer than their surroundings, rising due to their buoyancy. The Schwarzschild criterion for instability against convection

$$\nabla_{\text{rad}} > \nabla_{\text{ad}} , \quad (1)$$

is equivalent to the statement that convection will occur, when gas which is warmer than its surroundings is buoyant. The logarithmic gradients, $\nabla = d \ln T / d \ln p$, are labelled by the stratifications they apply to: “rad” for radiative equilibrium and “ad” for adiabatic.

These bubbles of gas are then envisioned to travel for one mixing length – hence the name of the formulation – before they dissolve more or less abruptly (Böhm-Vitense 1958). This picture has conceptual problems at the edges of convection zones or in small convective cores, where the distance to the edge is only a fraction of a mixing length. Most often, the convective elements are also ascribed an aspect ratio around unity, confounding the problem.

The mixing length is typically chosen to be $\ell = \alpha H_\rho$ or αH_p , where α is the main free parameter (of order unity) of the formulation, and H is the density or pressure scale height for locally exponential stratifications. It has also been suggested to use $\ell = \alpha z$, where z is the distance to the top of the convection zone (Canuto & Mazzitelli 1991, 1992). This choice would solve the conceptual problems listed above, but it introduces physical problems since there are strong reasons for real convection to have a stratification similar to an MLT model with $\ell = \alpha H_\rho$, as mentioned below.

There is also a notion of these convective bubbles travelling in a background of the average stratification. The concept of a background liquid is rather obvious, in this case, with isolated and distinguishable bubbles rising in it.

The 3D simulations of convection, on the other hand, display a very different phenomenon (see also Stein & Nordlund 1989; Nordlund & Stein 1997; Trampedach 2010). The convection consists of continuous flows; the warm gas rising almost adiabatically, in a background of narrower and faster downdrafts, forced by shear mass-conservation. A fraction of the upflows is continuously overturning in order to conserve mass on the back-drop of the steep and exponential density gradient.

Locally, the density, ρ , as function of depth, z , can be approximated by

$$\rho(z) \propto e^{z/H_\rho} . \quad (2)$$

When a vertical “column” of the upflow has travelled Δz , the column would therefore be over-dense by a factor of $e^{\Delta z/H_\rho}$, if the upflow were confined horizontally. There is of course no such confinement, and the fraction, $(e^{\Delta z/H_\rho} - 1) \rightarrow \Delta z/H_\rho$ for $\Delta z \rightarrow 0$, will overturn into the downdrafts.

The upflow will therefore be “eroded” by overturning, with an e -folding scale of H_ρ . The result of this concept is the same as that for the mixing-length picture described above (with $\ell = \alpha H_\rho$ and $\alpha = 1$), but without the same conceptual problems. Since the flows are continuous, including the overturning of upflows into the downdrafts, there are no discrete eddies of convection that should be much smaller than the scale of changes

in the atmosphere, as measured by H_p . An $\alpha > 1$ does therefore not pose a logical or physical inconsistency, as argued by, e.g., Canuto (2000). Many other inconsistencies of MLT remain, however.

Renaming it the erosion- or dilution-length formulation, it could be a first-order approximation to convection, as observed in the 3D simulations. This is the reason that the MLT formulation has worked so well despite its many short-comings: It is based on radial flows along a density gradient, under the constraint of simple mass conservation.

The above argument neglects vertical velocity gradients. A positive outward gradient accommodates more of the upflow and results in a smaller fraction of the upflow overturning. Accounting for the velocity gradients present in the simulations results in mixing lengths that are proportional to H_p rather than H_ρ , and discounts $\ell = \alpha z$, as shown by Trampedach & Stein (2011) for the same grid of simulations as used here. These actual scale heights of mass mixing deviate drastically from this proportionality in the surface layers, and are only loosely connected to the mixing length of the MLT formulation being calibrated in the present paper.

The 3D simulations also display a nearly laminar upflow, due to the density gradient smoothing out most of the generated turbulence. The downflows are narrower and faster, and since they work against the density gradient, they are also more turbulent. The downdrafts are not compressed adiabatically, since there is continuous entrainment of hot plasma from the neighbouring upflows. The downdrafts therefore remain super adiabatic to much greater depths than do the upflows which mainly become super adiabatic from radiative loss of energy around the local photosphere, $\tau \simeq 1$. There is also a lateral exchange of energy, extending the super-adiabatic peak in the upflow to larger depth than would have been the case with a purely vertical loss of radiative energy. This is also presented in Fig. 4 of Trampedach (2010). The super-adiabatic peak produced by the combination of these three phenomena is difficult to reproduce within the MLT framework (See Sect. 8.1).

Convective motions in the 3D simulations are prolific above the convection zone, with the velocity decreasing with a scale height which is larger than the pressure scale height. This introduces a new contestant in the atmosphere, and radiative transfer will have to compete with adiabatic cooling for the equilibrium stratification, as discussed by Nordlund & Stein (1991), Asplund et al. (1999), Collet, Asplund & Trampedach (2007) and in Paper I.

The asymmetry between upflows and downdrafts have some profound effects: In the photosphere, for example, the highly non-linear opacity, coupled with the large temperature contrast, results in a visible surface which is very undulated. Over the hot granules the $\tau \simeq 1$ surface is located at larger geometrical height than in the cooler inter-granular lanes, and the observed (disk-centre) temperature contrast is therefore much smaller than in a horizontal cross-section (Georgobiani, Stein & Nordlund 2003). This higher opacity in the granules causes a sub-photospheric heating of the granules (compared with a 1D calculation) which is not balanced by a corresponding cooling below the downflows, both because the opacity is

convex in temperature and because the downflows occupy a smaller fraction of the surface area. This introduces a *convective back-warming* on the geometrical scale, which has no counterpart on the optical depth scale (Stein & Nordlund 2003).

In the convective layers, the density and velocity differences between the upflows and the downdrafts give rise to a net kinetic energy-flux

$$F_{\text{kin}} = \frac{1}{2} \rho v^2 v_z, \quad (3)$$

which amounts to 10–30% of the total flux, depending on depth and stellar parameters. The assumption of symmetry in the MLT formulation, together with mass conservation, precludes such a kinetic energy-flux and is probably the biggest cause for disagreement with the simulations in the deeper, almost adiabatic part of the convection zone.

As convection approaches the adiabatic stratification, an actual theory of convection is not needed in the bulk of convection zones of more than a few pressure scale heights in depth. There we only need to determine which adiabat the convection zone is following. Since α is not fixed by the MLT formulation, the answer has to come from “outside” calibrations, e.g., through the classical matching of the radius of a solar model evolved to the present age (Gough & Weiss 1976), or as performed in the present paper, against realistic 3D convection simulations.

We will refer in the following to α as a measure of the efficiency of convection, but note here that the first-order term is already included in the MLT formulation. That term is the ratio of convective advection of energy to radiative diffusion of energy, known as the Peclét number which varies with depth and is essentially what is solved for in the cubic MLT equation. The primary MLT parameter, α , acts as a modulation of that first order convective efficiency provided by the Peclét number. Inherent in the MLT formulations is therefore a change in efficiency across the HR diagram, and within individual convective envelopes, with the least efficient convection to be found at the surface of main-sequence stars so warm that the convective envelope has almost disappeared. This, however, does not account for the fact that in real convection, small changes in the asymmetry between up- and downflows can greatly alter the transport properties of convection. Our calibration of α displays an amplification of MLT’s intrinsic decrease of convective efficiency with increasing T_{eff} (see Sect. 6).

Simulations in 2D are obviously attractive for their significantly lower computational cost, compared with 3D simulations. We advice caution, however, in interpreting both observations and phenomenological convection models in terms of 2D simulations. The morphology of 2D and 3D convection is fundamentally different, with 2D simulations being dominated by large-scale vortices which also increases the size of granules (Asplund et al. 2000; Ludwig & Nordlund 2000). In 3D vortices become diluted by the distance from their centres, and are consequently smaller and no longer the dominant feature of the flows.

Other approaches to convection in stellar models in-

clude two-stream models (Ulrich 1970; Nordlund 1976; Lesaffre, Podsiadlowski & Tout 2005), plume models (Rieutord & Zahn 1995), various closure models (Kuhfuß 1986; Canuto 1992; Chan & Sofia 1989; Kim et al. 1996), combinations of the latter two (Belkacem et al. 2006) and semi-analytical models informed by simulations (Rempel 2004).

3 THE SIMULATIONS

The fully compressible RHD simulations are described by Trampedach et al. (2013) and in Paper I, and the code is described in more detail in Nordlund & Stein (1990). General properties of solar convection, as deduced from the simulations, are discussed by Stein & Nordlund (1998). Among the code features important for the present analysis are radiative transfer with line-blanketing (Nordlund 1982; Nordlund & Dravins 1990), and the transmitting top and bottom boundaries. The bottom is kept at a uniform pressure (but not constant in time), to make a node in the radial p modes and minimize wave generation by the boundary conditions. The entropy of the inflowing plasma is evolved towards a constant which is adjusted to result in the desired effective temperature, and the velocities of the inflow are evolved towards a vertical flow that balances the mass-flux of the outflow. The outflows are left unchanged in all respects.

Each of the simulations were performed on a $150 \times 150 \times 82$ grid, equidistant and periodic in the horizontal directions, and optimized to resolve the photospheric temperature gradient in the vertical direction. The top boundary is located so that the maximum optical depth there is less than $\log \tau \lesssim -4.5$, and the bottom is located sufficiently deep for convection to be largely adiabatic—about seven pressure scale heights below the photosphere. The horizontal extent is chosen to cover of the order of 30 major granules. For the solar simulation this gives a simulation domain of $6 \text{ Mm} \times 6 \text{ Mm} \times 3.5 \text{ Mm}$ with 2.8 Mm below the photosphere.

Convection in the simulations consists of a warm, coherent upflow, with its entropy virtually unaltered from its value near the bottom of the convection zone. This asymptotic value of the entropy in the deep convection zone is shown in an *atmospheric* HR-diagram (having $\log g$ as the vertical axis) in Fig. 1 (also Fig. 1 of Trampedach et al. 2013), together with evolutionary tracks computed with the MESA code (Paxton et al. 2011). This S_{max} is also the value of the entropy fed into the simulations through the isentropic upflows at the bottom boundary. Because of the density gradient, mass conservation forces overturning of the upflows, on distances of the order of the density scale height, as mentioned in Sect. 2. The overturning plasma is entrained into narrow, fast and turbulent, entropy deficient downdrafts, generated by the abrupt cooling in the photosphere. Since only a small part of the convection zone is simulated, open boundaries are necessary for obtaining realistic results. With closed boundaries, the entropy deficiency and the turbulence would get recycled into the upflows, artificially reducing the asymmetry between upflows and downdrafts.

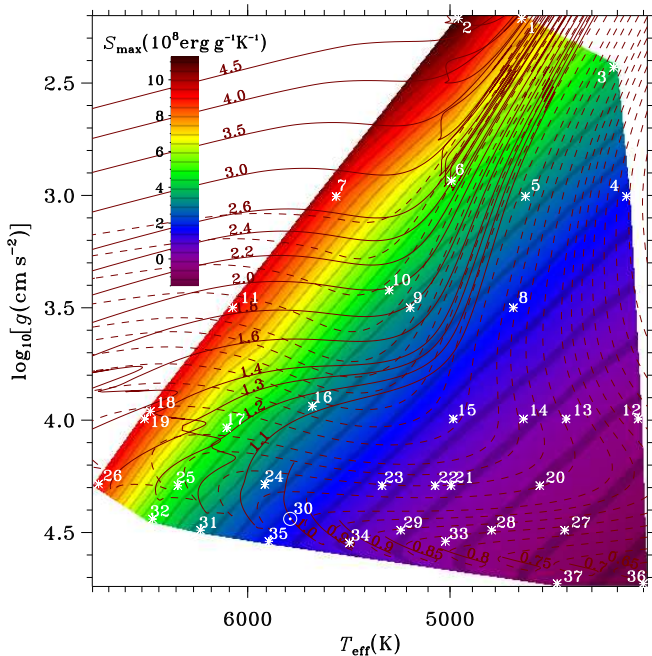


Figure 1. The asymptotic entropy (arbitrary zero-point), $S_{\max}/[10^8 \text{ erg g}^{-1} \text{ K}^{-1}]$, of the deep convection zone as function of stellar atmospheric parameters. This is also the entropy assigned to the inflows at the bottom of the simulation box. The T_{eff} -scale is logarithmic. We have also plotted stellar evolution tracks produced with the MESA-code (Paxton et al. 2011), with masses as indicated, to put the simulations in context. The dashed part shows the pre-main-sequence contraction, and α and initial helium abundance, Y_0 , were determined from a calibration to the present Sun. We interpolated the entropy linearly on Thiessen triangles (Renka 1984) between the simulations, and indicate the values with colours as shown on the colour bar. The location of the simulations is shown with white asterisks, except for the solar simulation which is indicated with a \odot . For this figure we also added the simulation numbers from Table 1.

Since spatial schemes of order higher than linear are unstable, artificial diffusion is needed. It can be argued that a Laplacian term in velocity with a constant viscosity would be the most physical choice, since it is the expected form of molecular diffusion. On the other hand, the dissipation-scale of atomic diffusion is many orders of magnitude removed from the smallest scales resolved by the simulations, making that argument tenuous at best. A Laplacian diffusion severely restricts the inertial range of hydrodynamic quantities, thus greatly affecting the transport properties of the plasma. Our simulations instead use a so-called hyper-viscosity scheme, which is tailored to only affect regions where it is needed and leave the rest untouched. This extends the inertial range without introducing spurious artifacts, pushing the dissipation scale towards the smallest scales resolved. In doing so, we loose contact with the various dimensionless numbers of hydrodynamics, but we consider that a small price to pay in return for a factor of about two in inertial range. Augustson et al. (2011) analysed a diffusion scheme conceptually similar to ours (in that it minimizes diffusion everywhere except where it is needed for stability) and

compared with the simple Laplacian form. Similar to our case, they found that at the same resolution, resolving power can be increased by a factor of two when Laplacian diffusion is abandoned.

Another requirement for comparison with observations is a realistic treatment of the radiative transfer in the atmosphere, and a corresponding quality of the atomic physics behind the opacities and the EOS. Compared with the simulations by Nordlund & Stein (1990), we have therefore employed the so-called MHD EOS (Hummer & Mihalas 1988; Däppen et al. 1988), updated most of the continuous opacity sources and added a few new ones, as mentioned in Paper I. The line opacity is supplied by opacity distribution functions (ODF) by Kurucz (1992a,b).

After relaxation to a quasi-stationary state, we calculated mean models for the envelope fitting (cf. Sect. 5). The temporal averaging was performed on a horizontally averaged column density scale, instead of a direct spatial scale, to filter out the main effect of the radial p modes excited in the simulations. We refer to this procedure as (*pseudo*) *Lagrangian averaging*, $\langle \dots \rangle_L$. A true Lagrangian average would be performed on the *local* column mass scale.

The simulations of the (irregular) grid are listed in Table 1 in the same order as the corresponding tables in Paper I and Trampedach et al. (2013), which is ascending in gravity and, for similar gravities, ascending in effective temperature. The spectral type is only meant as a guide, and none of our results relies on it. The simulations are run with constant gravity, which in 1D is referred to as the plane-parallel approximation (as opposed to spherical models), and are therefore independent of mass. The stellar masses listed in Table 1 are therefore not based on the simulations, but on the evolution tracks shown in Fig. 1. They are, however, used for the α calibration in Sect. 5, but the results are insensitive to the choice of mass with $\partial\alpha/\partial M \simeq 7 \times 10^{-4}$, with mass in units of M_\odot . The chemical composition is a modified Anders & Grevesse (1989) metal mixture, with helium and iron adjusted to correspond to the Grevesse & Sauval (1998) mix. This results in $X = 73.70\%$ hydrogen by mass and $Y = 24.50\%$ helium by mass, the latter in accordance with helioseismology (Christensen-Dalsgaard & Pérez Hernández 1991; Dziembowski, Pamyatnykh & Sienkiewicz 1991; Vorontsov, Baturin & Pamyatnykh 1991; Basu & Antia 1995; Richard et al. 1998). This also constitutes (1.26, 1.52 and 1.55 times) higher abundances of C, N and O than found in the solar abundance analysis by Asplund et al. (2009) based on a 3D solar simulation similar to ours. These elements, however, provide little opacity under the physical conditions of our simulations and we expect the abundance differences to have minor effects on our results, as also mentioned in Sect. 8.1 (the source of the so-called solar abundance problem (Bahcall et al. 2005) lies in the importance of the O opacity at the bottom of the solar convection zone). The detailed abundances are listed and further discussed by Trampedach et al. (2013).

Fig. 2 presents our simulation grid in the atmospheric HR-diagram, showing granulation snapshots of the simulations. The randomly selected snapshots are

Table 1. Fundamental parameters for the 37 simulations, and calibrated α 's and convection zone depths, d_{cz} , in units of stellar radius. The standard deviations describe the fluctuations in time.

sim	type	$T_{\text{eff}}/[\text{K}]$	$\log g$	M/M_{\odot}	α	d_{cz}
1	K3	$4\,681 \pm 19$	2.200	3.694	1.673 ± 0.024	0.49555
2	K2	$4\,962 \pm 21$	2.200	4.805	1.559 ± 0.025	0.28706
3	K5	$4\,301 \pm 17$	2.420	0.400	1.750 ± 0.021	0.97807
4	K6	$4\,250 \pm 11$	3.000	0.189	1.807 ± 0.020	0.99980
5	K3	$4\,665 \pm 16$	3.000	0.852	1.750 ± 0.020	0.91381
6	K1	$4\,994 \pm 15$	2.930	2.440	1.705 ± 0.021	0.51661
7	G8	$5\,552 \pm 17$	3.000	2.756	1.627 ± 0.021	0.22159
8	K3	$4\,718 \pm 15$	3.500	0.721	1.746 ± 0.023	0.81835
9	K0	$5\,187 \pm 17$	3.500	1.786	1.760 ± 0.028	0.51630
10	K0	$5\,288 \pm 20$	3.421	1.923	1.723 ± 0.029	0.43090
11	F9	$6\,105 \pm 25$	3.500	1.875	1.638 ± 0.027	0.11782
12	K6	$4\,205 \pm 8$	4.000	0.601	1.994 ± 0.032	0.76238
13	K4	$4\,494 \pm 9$	4.000	0.684	1.838 ± 0.018	0.65469
14	K3	$4\,674 \pm 8$	4.000	0.738	1.779 ± 0.024	0.60464
15	K2	$4\,986 \pm 13$	4.000	0.836	1.755 ± 0.022	0.52884
16	G6	$5\,674 \pm 16$	3.943	1.130	1.756 ± 0.034	0.34300
17	F9	$6\,137 \pm 14$	4.040	1.222	1.697 ± 0.025	0.19127
18	F4	$6\,582 \pm 26$	3.966	1.567	1.655 ± 0.020	0.06244
19	F4	$6\,617 \pm 33$	4.000	1.552	1.659 ± 0.020	0.05981
20	K4	$4\,604 \pm 8$	4.300	0.568	1.819 ± 0.023	0.50541
21	K1	$4\,996 \pm 17$	4.300	0.694	1.734 ± 0.022	0.44249
22	K1	$5\,069 \pm 11$	4.300	0.719	1.739 ± 0.027	0.43124
23	K0	$5\,323 \pm 16$	4.300	0.810	1.742 ± 0.024	0.39198
24	G1	$5\,926 \pm 18$	4.295	1.056	1.752 ± 0.029	0.26388
25	F5	$6\,418 \pm 26$	4.300	1.261	1.715 ± 0.030	0.13408
26	F2	$6\,901 \pm 29$	4.292	1.433	1.684 ± 0.038	0.03882
27	K4	$4\,500 \pm 4$	4.500	0.565	1.874 ± 0.016	0.41811
28	K3	$4\,813 \pm 8$	4.500	0.664	1.752 ± 0.022	0.38241
29	K0	$5\,232 \pm 12$	4.500	0.812	1.741 ± 0.020	0.33902
30	G5	$5\,774 \pm 17$	4.438	1.002	1.764 ± 0.030	0.27910
31	F7	$6\,287 \pm 15$	4.500	1.246	1.761 ± 0.036	0.16503
32	F4	$6\,569 \pm 17$	4.450	1.329	1.708 ± 0.021	0.10530
33	K1	$5\,021 \pm 11$	4.550	0.772	1.760 ± 0.024	0.34027
34	G9	$5\,485 \pm 14$	4.557	0.949	1.760 ± 0.024	0.29097
35	G1	$5\,905 \pm 15$	4.550	1.114	1.770 ± 0.027	0.23625
36	K6	$4\,185 \pm 3$	4.740	0.649	2.050 ± 0.027	0.33324
37	K4	$4\,531 \pm 10$	4.740	0.742	1.918 ± 0.040	0.29067

scaled by the logarithmic horizontal extent of each of the simulations—an extent which in turn is chosen to encompass about 30 major granules. The evolution tracks from Fig. 1 are added for reference.

4 THE ENVELOPE MODELS

The simulations were fitted to 1D, spherically symmetric envelope models (Christensen-Dalsgaard & Frandsen 1983) computed with a code closely related to the ASTEC stellar evolution code (Christensen-Dalsgaard 2008). The envelopes extend from a relative radius of $r/R = 0.05$, and out to an optical depth of $\tau = 10^{-4}$.

We used the same MHD EOS, and in the atmospheric part of the envelopes we used the same opacities, as in the convection simulations (see Paper I, Sect. 3.1). These atmospheric opacities are smoothly joined with the updated OP opacities (Badnell et al. 2005) between temperatures of $\log T = [3.95; 4.25]$ (where the differences are small and the models have nearly adiabatic convection; see also Fig. 2 of Paper I). These interior opacities were computed for the exact same composition as the atomic physics for the simulations as listed in Table 1 of Trampedach et al. (2013). This combined set of atmospheric and interior opacities are now included

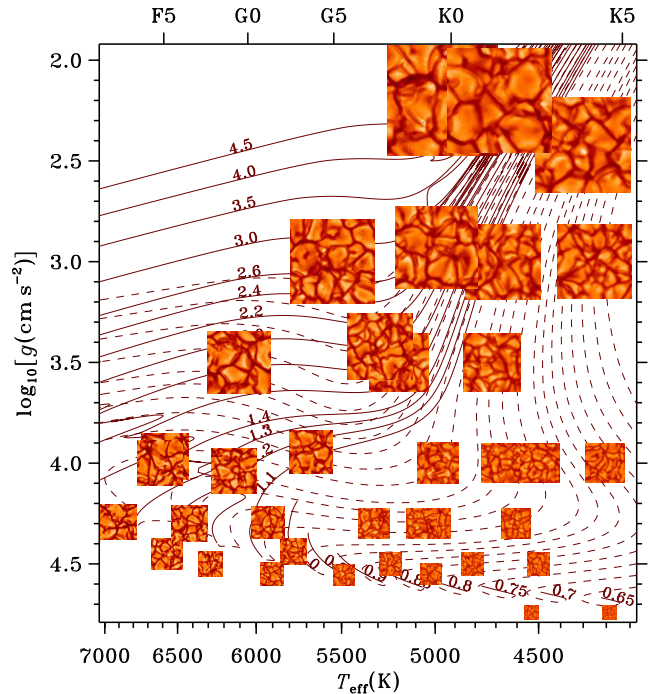


Figure 2. The position of the simulations in the atmospheric HR-diagram (with a logarithmic T_{eff} -axis). The simulations are represented by random snapshots of the disk-centre white light intensity. The size of these snapshots is proportional to the logarithmic width of the simulation domains. The evolutionary tracks are the same as shown in Fig. 1.

in the OPINT opacity interpolation package by Houdek & Rogl (1996), both of which can be downloaded from <http://phys.au.dk/~hg62/OPINT>.

Convection is treated using the standard MLT as described in Böhm-Vitense (1958), using the standard mixing length

$$\ell = \alpha H_p, \quad (4)$$

as supported by analysis of the same simulations by Trampedach & Stein (2011). We use form factors $\Phi = 2$ and $\eta = \sqrt{2}/9$ according to the notation of Gough (1977), with the values chosen to reproduce the original formulation by Böhm-Vitense (1958)¹. [See Ludwig, Freytag & Steffen (1999, App. A) for more details about the form factors. We use $f_1 = 1/8$, $f_2 = 1/2$, $f_3 = 24$ and $f_4 = 0$ in their notation].

The photospheric transition from optically thick to optically thin is treated by means of $T(\tau)$ relations derived from the simulations in Paper I. There we calculated temporal and τ (Rosseland optical depth) averaged temperatures, and reduced them to radiative equilibrium, T_{rad} , and computed generalised Hopf functions,

$$q(\tau) = \frac{4}{3} \left(\frac{T_{\text{rad}}(\tau)}{T_{\text{eff}}} \right)^4 - \tau, \quad (5)$$

as detailed in Paper I. This new formulation of the outer boundary ensures consistency between the $T(\tau)$ relation

¹ She brought up several values for the various form factors, but it is made clear which values she adopted in the end.

and the 1D model it is implemented in. It also applies throughout the stellar model, abandoning the artificial distinction between the atmosphere and the interior of a structure model, and renders moot the issue of where to switch between the two. We interpolate linearly in q between the simulations using a Thiessen-triangulation (Renka 1984) of the irregular grid in $\log_{10} T_{\text{eff}}$ and $\log_{10} g$. The point that we use individual $T(\tau)$ relations instead of scaled solar $T(\tau)$ relations is crucial for the present calibration, as discussed in Sect. 7.

All time-dependent and composition-altering processes, e.g., nuclear reactions, diffusion and settling of helium and metals, are left out of envelope models. This renders the envelopes functions of the atmospheric parameters, T_{eff} and g_{surf} (and composition) only, but it also rules out any abundance gradients. During stellar evolution, on the other hand, the net effect of radiative acceleration and gravitational settling, is for helium and metals to slowly drop out of the convection zone (Turcotte et al. 1998) building up an abundance gradient, just below the convection zone, which is smoothed out by chemical diffusion. As these processes are much slower than convection, the resulting abundance gradients are confined to below the convection zone, leaving our α calibration unaffected. The resulting depths of convection zones, on the other hand, *will* be affected by such abundance gradients. Radiative levitation in the atmosphere (Hui-Bon-Hoa et al. 2002) would segregate atoms and ions according to opacity, if it was not for the convective overshoot we see in our simulations, sustaining appreciable velocity fields and ensuring complete mixing, *at least* out to $\log \tau = -4.5$.

The pressure in the simulations is not purely thermodynamic; turbulent pressure also contributes to the hydrostatic equilibrium. We therefore include a turbulent pressure in the envelopes, based on the MLT convective velocities (see also Stellingwerf 1976)

$$p_{\text{turb},1\text{D}} = \beta v_{\text{conv}}^2 \varrho, \quad (6)$$

where β is a constant, adjusted as part of the calibration procedure, described in Sect. 5. For the calibration, we only need $p_{\text{turb},1\text{D}}$ from the matching point and into the interior, and we suppress it smoothly in the layers above. This has two reasons: The practical one is that most stellar structure calculations do not include such a turbulent pressure, and a calibration of α , including $p_{\text{turb},1\text{D}}$ in the whole convection zone, would not apply in these cases. The second, and more important reason, is that v_{conv} in MLT models displays a very sudden drop to zero at the top of the convection zone. In the standard solar model S of Christensen-Dalsgaard et al. (1996), the drop from a peak of 4 km s^{-1} occurs over just 72 km, corresponding to 0.42 pressure scale heights, H_p . Such a large velocity gradient will give rise to a devastating pressure gradient, causing nonphysical and sizable inversions in both density and gas pressure. This is shown in Fig. 3 for our simulation with the most vigorous convection, the 6900 K dwarf, No. 26 in Table 1. From that figure we see that not suppressing p_{turb} at the surface causes a gas pressure inversion, not seen in the simulations, as well as a much increased density inversion. To include this full 1D turbulent pressure, we had to limit the form-factor of

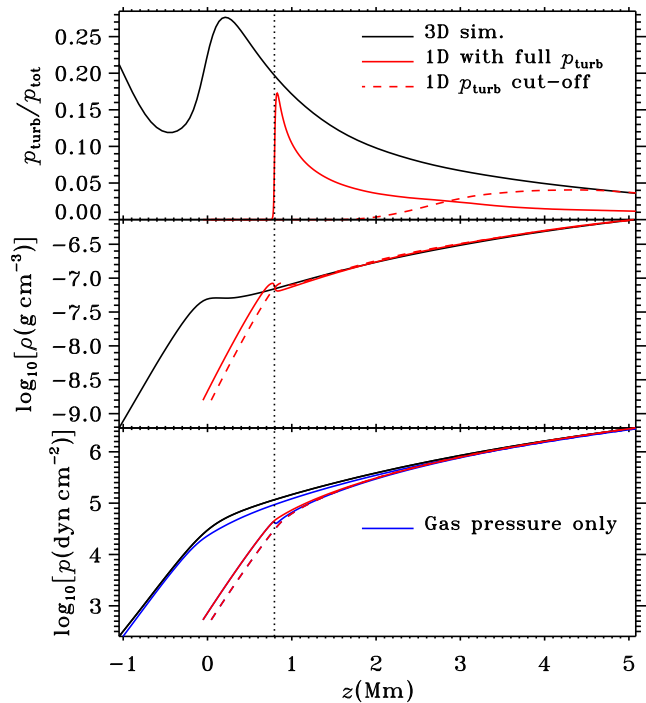


Figure 3. Comparing the structure of the $T_{\text{eff}} = 6901 \text{ K}$, $\log g = 4.292$ 3D convective atmosphere in solid black, and some 1D counterparts in red. The three panels show turbulent to total pressure ratio, logarithmic density and logarithmic pressures as function of depth. The red dashed lines show the 1D envelope model calibrated to the 3D simulation. The turbulent pressure is suppressed towards the surface, as is evident from the top panel. The solid red line shows a similar 1D model, but without this suppression of p_{turb} , and with $\beta = 0.260$, as opposed to the calibrated 0.804. In the bottom panel the gas pressure is shown in blue.

equation (6) to $\beta = 0.260$, as opposed to $\beta = 0.804$ from the calibration. This is seen in the top panel as a lack of convergence to the 3D result with depth. If a model with the more realistic value of β could converge, the turbulent pressure would be the dominant contributor, at 53.4% of the total pressure. The local pressure scale height at the turbulent pressure peak is about 0.8 Mm, and the drop from that peak to zero occurs in under 15% of that. To enable integration of hydrostatic equilibrium, it is therefore necessary to introduce some cut-off for $p_{\text{turb},1\text{D}}$. We have constructed this to be smooth and gradual (small gradient) and deep, just above the matching point, minimizing its effect on the models.

In the 3D simulations, on the other hand, turbulent pressure peaks about half a pressure scale height below the top of the convection zone, drops off smoothly both above (from convective overshooting) and below and is non-zero at all depths. The maximum (with depth) of the turbulent to total pressure ratio is shown in Fig. 3 of Trampedach et al. (2013), and that quantity is a good measure of how vigorous the convection is. For the Sun, that ratio is 13.75%.

We recommend not including a 1D-turbulent pressure which is confined to the convection zone, since it will exhibit unphysically large and damaging gradients

at the top of the convective envelope (see Fig. 3). Baker & Gough (1979) noted that the turbulent pressure, if included consistently (in all terms), increases the order of the equations for the structure of the envelope model from three to four. They further found that without overshoot the transition to the non-convective case at the boundaries of the convection zone gives rise to singularities which have proved very difficult to treat numerically. Most non-local and/or time-dependent, MLT-style descriptions of convection also accommodate overshooting (Spiegel 1963; Shaviv & Salpeter 1973; Nordlund 1974; Ulrich 1976; Gough 1977; Eggleton 1983; Grossman 1996; Grigahcène et al. 2005), and some of these have the correctly negative convective flux in the overshoot region. Most of these still have a strong and direct connection between velocities and fluxes, meaning that the velocities still fall off to sharply, producing unphysically large gradients in turbulent pressure, or alternatively, producing too extended a flux transition from convection to radiation (see also Renzini 1987, for further analysis). The reason for this is the assumed constancy of the fractional area occupied by each direction of convective flows, f_{up} and f_{dn} , and the often assumed symmetry of these: $f_{\text{up}} = f_{\text{dn}} = 1/2$. Some of these models have positive convective fluxes in the overshoot region because they mainly consist of a smoothing of quantities over some length scale. In our simulations the negative convective overshoot flux is due to a reversal in temperature change in response to a radial displacement, with the upflows getting cooler than the downflows. Our simulations do not address the issue of overshooting at the bottom of convective envelopes, but one could argue that a successful model for overshooting should also be able to reproduce, at least qualitatively, our results for overshoot into the atmosphere. Overshooting from convective cores and the bottom of convective envelopes is crucial for various stages of stellar evolution and an improved understanding is much needed.

Well below the super-adiabatic top of the convection zone, $p_{\text{turb,1D}}$ does match the turbulent pressure of the simulations rather well, giving an almost differentiable match. This is part of our evidence that envelope models including $p_{\text{turb,1D}}$, with β and α fitted as described in Sect. 5, give a realistic extension of the simulations towards the centre of the star. This fact was exploited in an investigation of convective effects on the frequencies of solar oscillations (Rosenthal et al. 1999) by analysing eigenmodes in a model combining the simulation and a matched envelope model. This same procedure was also employed in a calculation of p-mode excitation (Stein et al. 2005, 2007) for a range of stars. We can now proceed with the matching, with confidence.

5 MATCHING TO ENVELOPE MODELS

In order to derive α values from the simulations we matched 1D envelope models to horizontal and temporal averages of the 3D simulations at a common pressure point deep in the simulation. The matching is performed by adjusting β , equation (6), until the 1D-turbulent pressure agrees with that of the simulation, and α until the

temperatures agree, while keeping the mass and luminosity of the envelope constant. The masses, as listed in Table 1, are chosen based on the atmospheric parameters of evolution tracks constructed with the MESA-code (Paxton et al. 2011), calibrated to the present Sun as per usual (Gough & Weiss 1976). The luminosity follows from this mass and the atmospheric parameters of the simulations. These masses are obviously inconsistent with our calibration, but our calibration is also insensitive to this choice of mass, with $\partial\alpha/\partial M \sim 0.001$.

This method demands a high degree of consistency between the simulations and the envelope models at the matching point, which is the reason for using the exact same EOS (and chemical composition) in both cases, and for including a turbulent pressure in the deep part of the envelope models. The depth of the matching point is chosen for each simulation as a trade-off between minimizing boundary effects (which increase with depth), and minimizing fluctuations in thermodynamic quantities (which decrease with depth). The latter is to ensure that the mean ρ , T and p_{gas} are related by the EOS, i.e., that direct 3D-effects are negligible, as is of course always the case in 1D models. In all our cases, the matching point is located deeper than $\log \tau = 4$, and at pressures at least 100 times larger than in the photosphere.

In order to filter out non-convective effects from this calibration of α , we also demand consistency between 1D and 3D in the treatment of radiative transfer in the atmosphere. We accomplish this by using the Rosseland opacities and the $T(\tau)$ relations from the 3D simulations, in the atmospheres of the 1D envelope models (see Paper I for details).

We also note that the common pressure point between the averaged 3D simulation and 1D model, being located deep in the simulation, means that the two models generally will disagree on the location of the surface, R , of the star (where $\langle T \rangle = T_{\text{eff}}$). This is due to the convective expansion of 3D atmospheres compared with 1D, as discussed by Trampedach et al. (2013). The 1D envelopes therefore have slightly smaller radii (by up to a per cent of the stars radius for the warmest giant and by as little as 10^{-5} for the coolest dwarf), and hence slightly larger T_{eff} and $\log g$, when the 3D simulation and 1D envelope are constrained to have identical mass and luminosity.

The main advantage of our method for calibrating the MLT α is the resulting combined models of averaged 3D simulations outside the matching point and the calibrated 1D envelope model interior to the matching point. Our method ensures these combined models are continuous, and they can therefore be used for computing various asteroseismic quantities, which can then be interpolated in the grid of simulations. Such combined models have been used by Rosenthal et al. (1999) to estimate the helioseismic surface effect, i.e., systematically overestimated model frequencies due to shortcomings at the surface of 1D solar models. They have also been employed in a calculation of p-mode excitation for a range of stars (Stein et al. 2005; Samadi et al. 2007; Stein et al. 2007), based on the formulation by Nordlund & Stein (2001); Stein & Nordlund (2001). Such calculations are also planned for our grid of simulations and α calibrated 1D models pre-

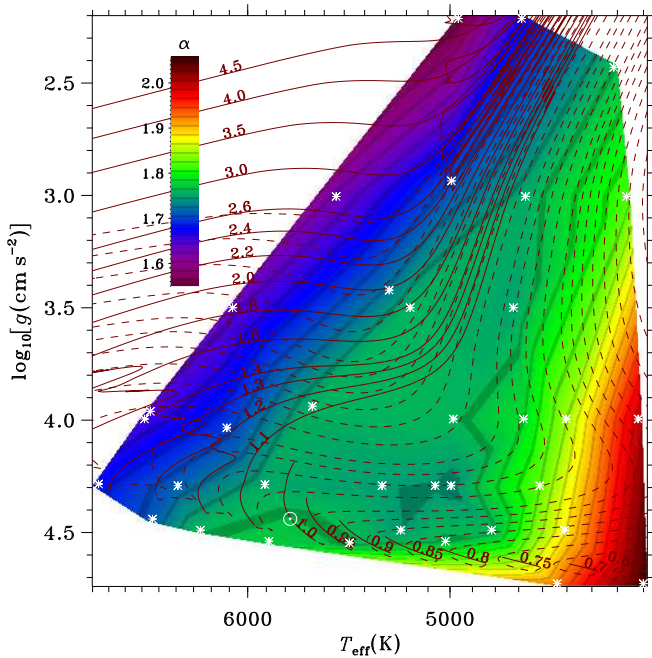


Figure 4. As Fig. 1, but showing the behaviour of α with T_{eff} and g_{surf} . The over-plotted evolutionary tracks cover the mass-range $0.65\text{--}4.5 M_{\odot}$, as indicated. The solar simulation is indicated with a \odot and the locations of the other simulations, as listed in Table 1, are shown with asterisks.

sented here. The method used by LFS, of matching to the entropy of the adiabat, does not ensure such continuous matching of 1D interior and averaged 3D atmospheres and complicates their use for asteroseismic applications. Their method does, however, ensure the correct location of the bottom of the convective envelope as determined by the Schwarzschild criterion. The two methods will converge with deeper matching point of our method, as the stratification approaches the adiabat exponentially.

6 RESULTS

In Fig. 4 we show the results of this calibration of the MLT α as function of effective temperature and gravity. The corresponding atmospheric entropy jump is shown in Fig. 4 of Trampedach et al. (2013). We also list these calibrated α values in Table 1 together with their standard deviations, from performing the envelope matching to individual time-steps of the horizontally averaged simulations. This scatter in α ranges between 0.015 and 0.040, with an average of 0.026. The standard deviations listed for T_{eff} is likewise from the fluctuations in time. In Table 1 we also list the resulting depths of the convective envelopes, d_{cz} , relative to the stellar radii.

In Fig. 5 we show our calibrated α values as function of T_{eff} , with error-bars corresponding to the RMS scatter in T_{eff} and α . The local $\log T_{\text{eff}}$ -gradient of $\alpha(T_{\text{eff}}, g)$ is indicated with line-segments,

Our α calibration results in low values along the warm edge of our grid, which is approaching the end of convective envelopes from the cool side of the HR dia-

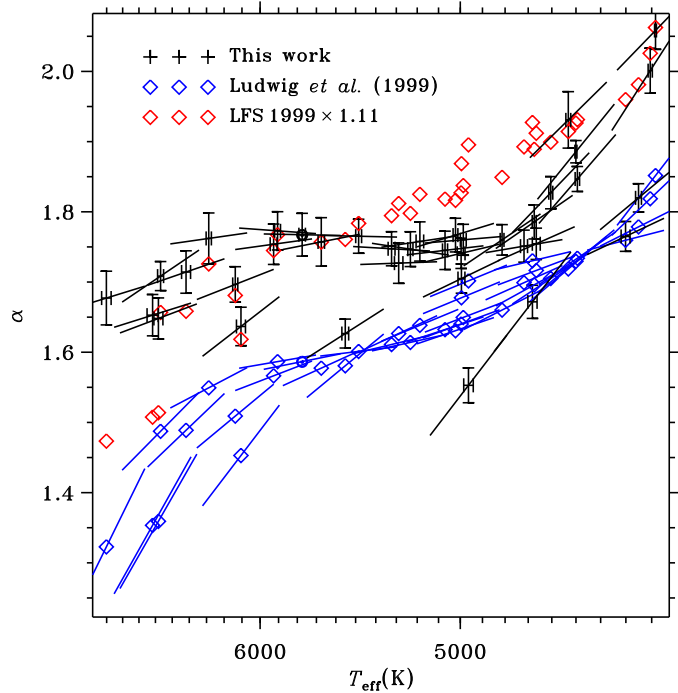


Figure 5. A plot of the values of α found from our matching procedure (with gradient-lines, showing the local slope in $\log T_{\text{eff}}$, and error-bars in both T_{eff} and α), compared with the calibration against 2D simulations, performed by Ludwig, Freytag & Steffen (1999) (lower, blue diamonds with gradient lines). We have also multiplied their result by 1.11 to agree with our result for the Sun (upper, red diamonds, no gradient lines).

gram. The depth of convective envelopes decreases as this edge of our grid is approached, as does the convective efficiency, quantified by α . The highest α values are found in the coolest dwarfs, spanning the range from $\alpha = 1.68$ to 2.05 on the main sequence. A $0.7 M_{\odot}$ -star would experience the largest change in α over its life-time (about 0.15), whereas $0.8\text{--}1.1 M_{\odot}$ stars find themselves on a triangular plateau of $\alpha \sim 1.76$, spanning a temperature range of $T_{\text{eff}} \sim 4800\text{--}6000$ K along the main sequence and going up to $\log g \simeq 3.0$. This feature was also noted by LFS. This plateau encompasses the evolution so far of the Sun, as well as the nearest and best constrained binary, α Cen A and B (the C component is too cool to be covered by our grid of simulations), which means that the evolution of these three stars is well described by a single value of $\alpha = 1.76 \pm 0.01 \pm 0.03$ (\pm range, \pm uncertainty of calibration).

Stars ascending the giant branch essentially follow iso- α curves, so here α is a function of mass and approximately constant with age. The values here range from 1.56 for a $4.3 M_{\odot}$ -star to 1.75 for $0.84 M_{\odot}$. Stars more massive than about $1.25 M_{\odot}$ experience a significant increase in α during their evolution, but most of that change occurs in the Hertzsprung gap of fast evolution. Effectively they have a small α on the main sequence and a larger α on the giant branch. Bear in mind, however, that our grid of simulations only covers up to $1.4 M_{\odot}$ on the main sequence.

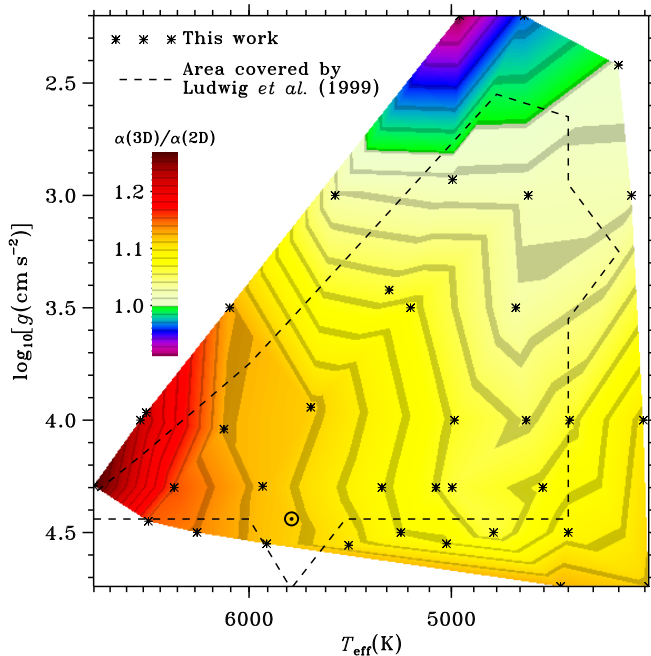


Figure 6. A comparison between the present α calibration and that by Ludwig, Freytag & Steffen (1999) in the T_{eff} -/ $\log g$ -diagram. The area covered by their simulations is shown with the dashed outline, and outside this, their fit which was used for this plot is an extrapolation.

6.1 Comparison with Ludwig, Freytag & Steffen (1999)

The calibration of α against 2D RHD simulations performed by LFS employed a method completely independent of ours. In Fig. 5 we have displayed their fit to their results, as applied to the atmospheric parameters of our simulations (lower set of blue \diamond 's, with line-segments indicating their local $\log T_{\text{eff}}$ -derivatives). They suggest a scaling of their results by 1.1–1.2 to translate from 2D to 3D, and we note the profound morphological differences between 2D and 3D atmospheric convection, as discussed by Asplund et al. (2000). LFS also recommend that in order to match 1D solar structure models to the present age Sun, modellers should use the LFS α calibration differentially, scaling it by their α_{\odot} . We fully adopt that recommendation, with the caveat that the $T(\tau)$ relations and atmospheric opacities of the 3D simulations should be used alongside our α calibration. We expect this procedure to result in a minimal need for scaling, but would be most interested in hearing of contrary experiences.

Our results do indeed agree with LFS's in the solar vicinity, after a scaling by 1.11, as shown by the upper set of red diamonds in Fig. 5. The disagreement around $T_{\text{eff}} = 4800$ K is most likely also due to differences in the opacities. They based their opacities on the Atlas6 line opacities whereas we use the somewhat newer Atlas9 line opacities (in the form of opacity distribution functions). The difference, as outlined by Kurucz (1992c), consists of the addition of molecular opacity (hydrides and CN, C₂ and TiO) and improved calculations for the iron-group elements – all in all a factor of 34 more molecular, atomic and ionic lines.

These opacity changes should affect the hotter stars the least, but they still have an effect on the solar model – that was, after all, the main motivation behind the opacity updates (Kurucz 1992b). We therefore suspect that the scaling factor, translating LFS' results from 2D to 3D should be based on the hotter stars. But there are also other differences between our simulations: LFS used grey radiative transfer in the bulk of the 58 2D simulations going into their analysis, adding another systematic difference (also generally decreasing with T_{eff}) between our results. Furthermore, they used the old pre-helioseismology value of the helium abundance, $Y = 28\%$, which effectively lowers the atmospheric opacity, compared with ours (the He, being an inert gas, displaces high opacity species, as well as electron donors for H⁻ formation).

The ratio between the two calibrations is also shown in an atmospheric HR diagram in Fig. 6, which also shows the extent of LFS's grid. From this plot it is clear that most of our simulations have α values exceeding those of LFS's 2D simulations, except for giants with $\log g \lesssim 2.5$. Our warmest giant has $\alpha(3D)/\alpha(2D) = 0.92$ but is also an extrapolation from LFS's grid. The maximum, for our warmest dwarf which is also within their grid, is 1.27.

It seems natural to expect that quantities other than T_{eff} and g_{surf} would be more relevant for describing the efficiency of convection. The optical depth at the top of the convection zone, for example, seems much more relevant and directly related to the issue, or the peak amplitude of the turbulent to total pressure ratio, or the Mach number as suggested by Samadi et al. (2013). These quantities as well as others we have tested, do not provide simpler or single-valued functions for α , and the scatter is large than the individual σ_{α} . We conclude that two independent variables are necessary to describe α , and we naturally choose T_{eff} and $\log g$.

6.2 Gravity darkening of slowly rotating stars

A slowly rotating star can, as a first-order approximation, be described as a set of 1D stellar models with outer boundary conditions that depend on co-latitude, θ , as $T_{\text{eff}}(\theta)$ and $g_{\text{eff}}(\theta) = g - R\Omega^2 \sin \theta$, where R is the radius of the star and Ω is the (uniform) rotation rate. A formulation was developed by von Zeipel (1924) for stars in radiative equilibrium, and a main finding² was that $T_{\text{eff}} \propto g^{0.25}$.

Building on this, Lucy (1967) extended the formulation to also apply to convective envelopes, assuming that the various latitudes are connected in the deep convection zone by a common adiabat. The generalisation of von Zeipel's result is $T_{\text{eff}} \propto g^{\beta}$, defining the *gravity-darkening* exponent β . In case of convective envelopes and under the common-adiabat assumption, this gives rise to the adiabatic gravity-darkening exponent

² Whether his result is predicated on the assumption that the opacity is of the form $\kappa_{\text{Ross}} = f(pT^{-4})$ (compared with the actual $\kappa_{\text{Ross}} \propto \rho T^9$), is not clear and is beyond the scope of the present work.

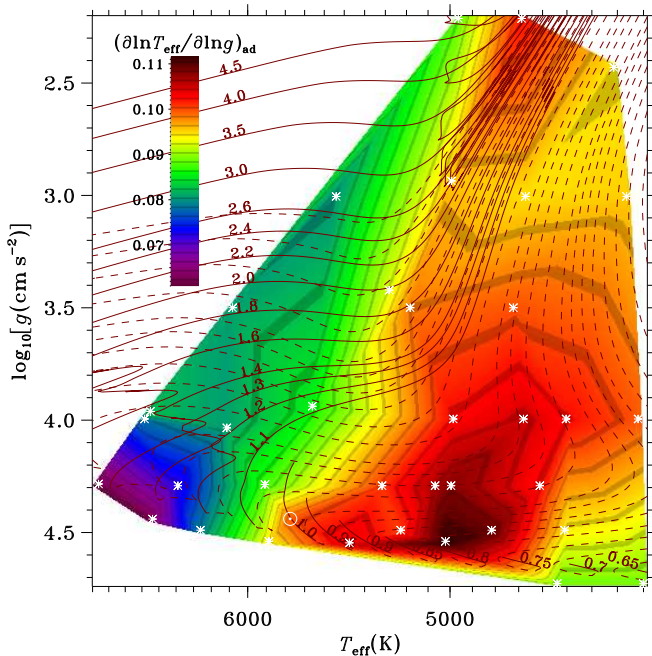


Figure 7. As Fig. 1, but showing the gravity-darkening exponent, β_{ad} , found from differentiating the asymptotic adiabats of Fig. 1.

$$\beta_{\text{ad}} = \left(\frac{\partial \log T_{\text{eff}}}{\partial \log g_{\text{eff}}} \right)_{\text{asympt, ad}}. \quad (7)$$

We have evaluated β_{ad} by finding the slopes of the adiabats in Fig. 1, as shown in Fig. 7. The values we find are similar to the value, $\beta_{\text{ad}} \sim 0.08$, which was originally suggested by Lucy (1967), and also agrees with the values reported by LFS although we seem to find a larger range.

The Sun, with an equatorial rotation rate of 450 nHz, displays an equatorial $\log_{10} g_{\text{eff}}(\theta = 90^\circ)$ that is a mere 8.82×10^{-6} dex smaller than at the poles. Making the above assumption of a common adiabat of the deep convection zone, and using $\beta_{\text{ad}, \odot} = 0.100$ from Fig. 7, results in the equator being an unobservable 12 mK cooler than the pole (a contrast of 2.1×10^{-6}).

On the other hand, it is also quite likely that meridional flows in stars will build up an entropy gradient with latitude, as suggested by Miesch, Brun & Toomre (2006). If we take a latitude-independent T_{eff} as the other extreme of possibilities, we get an entropy contrast in the solar convection zone of 1.60×10^{-6} . This is similar to the range of contrasts, $0.95\text{--}4.73 \times 10^{-6}$, explored by Miesch, Brun & Toomre (2006) to obtain the observed solar differential rotation in a 3D simulation of the deep solar convection zone.

Rotational effects are obviously much more important for many other stars. Also in this regard has NASA’s *Kepler* mission provided a treasure trove of observations, with several recent calculations of rotation periods from spot-modelling of planet candidate host stars by Walkowicz & Basri (2013), McQuillan, Mazeh & Aigrain (2013), of 12 000 other F–M *Kepler* targets by Nielsen et al. (2013) and of 34 000 *Kepler* main-sequence targets cooler

than 6 500 K by McQuillan, Mazeh & Aigrain (2014) with periods down to 0.2 days.

For fast rotators, more elaborate models are needed [See, e.g., Espinosa Lara & Rieutord (2011) for analytical 2D work and Augustson et al. (2012) for 3D hydrodynamics simulations], but the behaviour of $S_{\text{max}}(T_{\text{eff}}, \log g)$ in Fig. 1 should still be relevant for such modelling.

7 IMPLICATIONS FOR STELLAR STRUCTURE

In this section we explore the effects of outer boundary conditions on the 1D structure models, introduced in Sect. 4. We evaluate sensitivities to changes in α , $T(\tau)$ relations and atmospheric opacities in Sect. 7.1 and employ the $T(\tau)$ relations of Paper I, together with other commonly used choices, in Sect. 7.2, commenting on the effects on the depths of convective envelopes. This analysis does not include calibrations of α , but address how global properties of 1D models react to independent changes to κ_{atm} , $T(\tau)$ relation and α .

The reason for convection zones growing with increasing convective efficiency, α , is found in Sect. 7.4.

7.1 The depth of outer convection zones

The depth of an outer convection zone depends in a complex way on the surface boundary conditions. With some simplifications, however, a rough idea of the mechanisms involved can still be obtained. We convert the equation of hydrostatic equilibrium from the conventional height scale to an optical depth scale

$$\frac{dp}{d\tau} = \frac{g}{\kappa}, \quad (8)$$

and integrate inward from $\tau = 0$ to get the pressure with depth. For the present discussion we only need the differential response to changes in the atmosphere and the precise values of the quantities are immaterial. We therefore write the pressure in the photosphere

$$p_{\text{ph}} = \frac{g}{\bar{\kappa}} \bar{\tau}, \quad (9)$$

as a one-step numerical integration from $p = 0$ to p_{ph} and $\tau = 0$ to $\bar{\tau}$, where $\bar{\kappa}$ and $\bar{\tau}$ are some appropriate averages over the atmosphere. This results in a first-order estimate of the effects of changing various parts of the physics in the atmosphere.

Using some average of the inverse $T(\tau)$ relation for $\bar{\tau}$, a relation between T and p is obtained. An increase in $T(\tau)$ will decrease $\tau(T)$, as the $T(\tau)$ relation is monotonically increasing, and will therefore have the same decreasing effect on p as will an increase in the opacity. Changes to the $T(\tau)$ relation are performed on the generalised Hopf functions, equation (5), which are normalised by the surface flux.

We will now assume that an atmospheric pressure change [due to changes to κ_{atm} or $q(\tau)$], represents the same factor of pressure change throughout the convection zone. The change in the depth of the convection zone can be derived from the response to such a pressure change at the bottom of the convection zone. The Schwarzschild

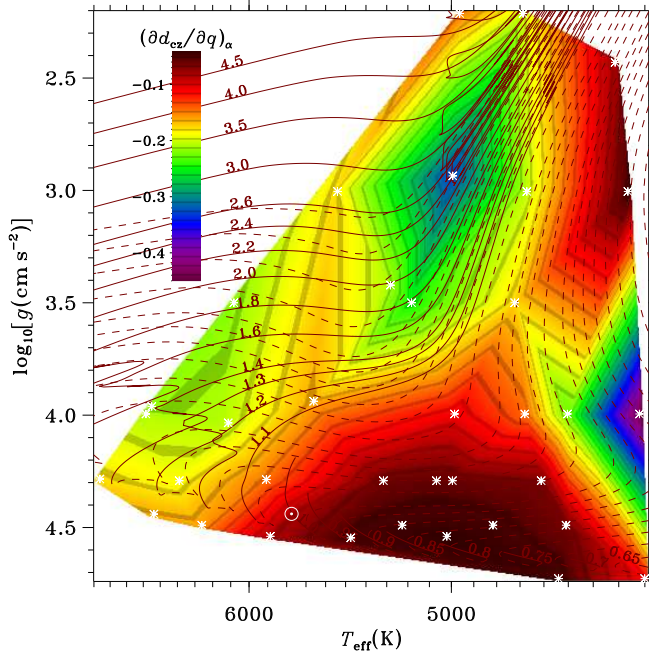


Figure 8. As Fig. 1, but showing the differential response of the depth of the convection zone in units of stellar radii, R , to a change in the $T(\tau)$ relation, using $\delta q = 5 \times 10^{-3}$. Our simulations all display shallower convective envelopes with increasing q .

criterion for convection to occur, equation (1), is mainly governed by ∇_{rad} , as the adiabatic gradient is very close to the ideal- and fully-ionised-gas value of $\nabla_{\text{ad}} = \frac{2}{5}$ at the bottom of deep convection zones.

In the deep interior, where the Hopf function, equation (5), is constant and the turbulent pressure is insignificant, the radiative temperature gradient is

$$\nabla_{\text{rad}} = \frac{3}{16\sigma} \frac{\kappa F_{\text{tot}} p}{g T^4}. \quad (10)$$

This gradient will decrease with a decrease in pressure and the bottom of the convection zone will therefore move outward. Since ∇_{rad} depends strongly on temperature and has a steep gradient at the bottom of the convection zone, the pressure change hardly affects the location of $\nabla_{\text{rad}} = \nabla_{\text{ad}}$ on the temperature scale. The largest effect is therefore due to the (almost unchanged) temperature at the bottom of the convection zone occurring at a smaller pressure.

This trend is confirmed by the experiments. We calculated envelope models with small (additive) changes (0.005) to α , q and the atmospheric opacity, $\ln \kappa_{\text{atm}}$ in order to find the differential changes to the relative depth d_{cz} (in units of stellar radius, R) of the convection zone. The fundamental parameters, T_{eff} , g_{surf} and M (and hence also R and L) were held constant between the experiments. Keeping T_{eff} constant effectively anchors the temperature structure so that the effect of the perturbations in α , q and $\ln \kappa_{\text{atm}}$ give similar magnitude responses in q and p (and close to constant in the convective envelope) and an order of magnitude smaller response in T .

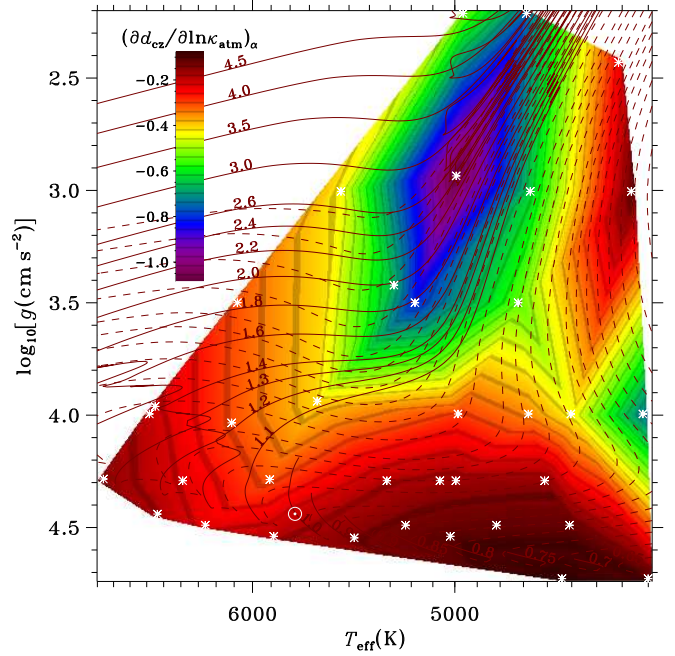


Figure 9. As Fig. 1, but showing the differential response of the depth of the convection zone, to a change in the atmospheric opacity, $\delta \ln \kappa_{\text{atm}} = 5 \times 10^{-3}$. All our simulations have shallower convective envelopes with increasing $\ln \kappa_{\text{atm}}$.

The results of these experiments are presented in Figs. 8–10, in the form of changes to the depth of the convective envelope, as function of the atmospheric parameters T_{eff} and $\log g$. Our experiments shows that both $\partial d_{\text{cz}}/\partial q$ in Fig. 8 and $\partial d_{\text{cz}}/\partial \ln \kappa_{\text{atm}}$ in Fig. 9 are negative and have a similar functional form so that $\partial d_{\text{cz}}/\partial q \simeq 0.4 \times \partial d_{\text{cz}}/\partial \ln \kappa_{\text{atm}}$. The depth of the convection zone increases with increasing α , as expected (see Sect. 7.4), and we have approximately $\partial d_{\text{cz}}/\partial \alpha \simeq -0.7 \times \partial d_{\text{cz}}/\partial \ln \kappa_{\text{atm}}$.

The convective flux in the MLT formulation may be written as

$$F_{\text{conv}} \propto \alpha^2 \frac{p_g^2}{T^{3/2}} (\nabla - \nabla')^{3/2}, \quad (11)$$

where ∇' is the temperature gradient in the upflowing convective elements and ∇ is the average of the gradient between the up- and downflowing elements. Note that this is all in the 1D mixing-length picture, so the average gradient ∇ , is not the average of a 3D quantity which would have been denoted by $\langle \nabla \rangle$. The difference between ∇ and ∇' is almost equal to the superadiabatic gradient, $\nabla - \nabla_{\text{ad}}$. Based on equation (11), an increase in temperature and/or a decrease in pressure (brought about by changes to the $T(\tau)$ relation or the atmospheric opacity) will therefore be accompanied by an increase in $\nabla - \nabla_{\text{ad}}$ in order to maintain the total flux (and the fixed T_{eff} of the model). This increase of $\nabla - \nabla_{\text{ad}}$, corresponding to a decrease of the efficiency of the convection, will lead to a smaller convection zone. The effect can be counteracted by increasing α , which increases the convective efficiency by increasing the distance travelled by convective elements. An increase in the efficiency of convection will enlarge the convection zone, as seen from Fig. 10 (see

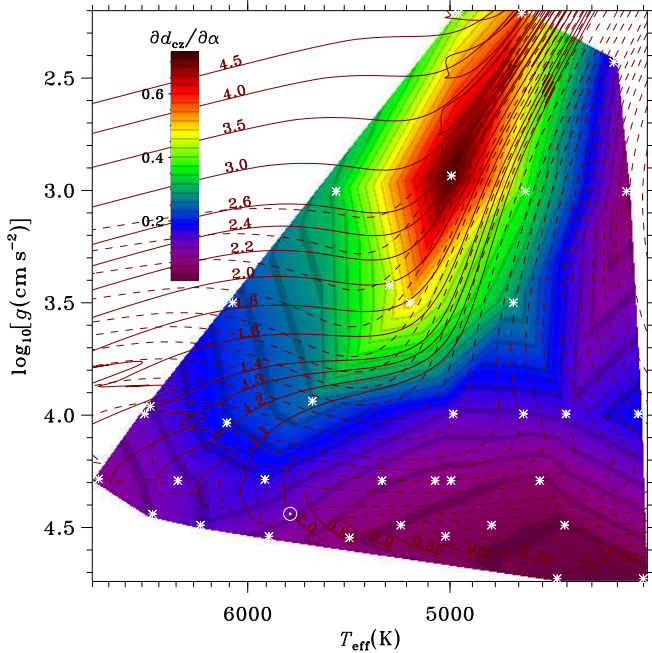


Figure 10. As Fig. 1, but showing the differential response of the depth of the convection zone, to a change in the convection parameter, $\delta\alpha = 5 \times 10^{-3}$. All our simulations display a deepening of their convective envelopes with increasing α , as expected.

also Sect. 7.4 below).

As far as global observables are concerned, uncertainties in the atmospheric opacities, line-blocking and mismatches between the τ scale and the grey opacity may be hidden in α together with pure convection effects. This is one reason that so many values for the solar α can be found in the literature (another reason being the lack of consensus on the values for the auxiliary MLT parameters). As illustrated by Figs. 8–10, such flaws in the treatment of the photosphere will not have the same effect on all stars and an incorrect differential behaviour would be expected from such a solar calibration, masking real convection effects (i.e., an α that varies with atmospheric parameters).

Since it is customary to use a solar-calibrated α for computing stellar models, we have also computed a set of envelopes with constant $\alpha = \alpha_{\odot}$, but still using the individual $T(\tau)$ relations. The effect of this is to overestimate the fractional depth of the convection zone of giants by 4–8% and underestimate it for cool dwarfs by about 1%, as shown in Fig. 11. This effect is somewhat counteracted when also keeping the $T(\tau)$ relations constant (scaled solar). The result of Fig. 11 is then further changed by a reduction of d_{cz} along the warm edge of our grid by 1.7% and an increase of d_{cz} by about 5% along the cool edge.

7.2 Effects of changing the $T(\tau)$ relations

Since there currently are a number of schemes for using $T(\tau)$ relations in stellar models, we find it worthwhile to explore the consequences of a few of these. We have kept

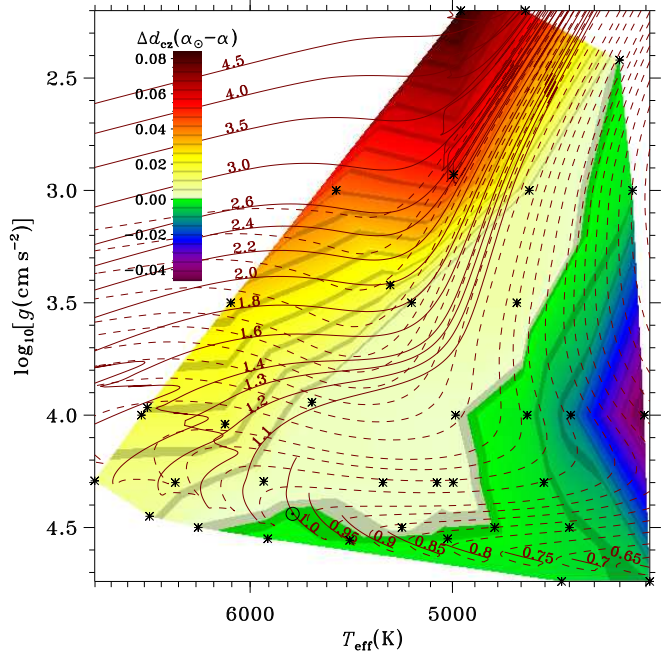


Figure 11. As Fig. 1, but showing differences in the depth of the convective envelope between models using solar-calibrated and individually calibrated values of α , in the sense that warm giants with α_{\odot} have deeper convective envelopes.

the opacity and the mixing length, α , unchanged in the experiments below.

As mentioned earlier, one of the first solar $T(\tau)$ relations to be published (Krishna Swamy 1966), is still in wide-spread use in stellar models. Fig. 12 shows the effect of using this $T(\tau)$ relation (scaled to the stellar T_{eff}) instead of the individual ones found from the simulations. The effect is largest for a $\sim 4.5 M_{\odot}$ star on the horizontal branch (HB), or a slightly more massive star approaching the Hayashi line after crossing the Hertzsprung gap, which has its convection zone decreased from 28% to 21% of the stars radius, from employing the Krishna Swamy $T(\tau)$ relation. The smallest effect (apart from the fully convective No. 4) is found in the cool dwarf corner of the HR diagram (simulation No. 36 of Table 1), where the convection zone depth is only decreased from 33.3% to 33.0%. The solar convection zone shrinks from 27.9% to 25.2% of R_{\odot} , from this change.

Another common approximation is to use a scaled solar $T(\tau)$ relation, albeit a more modern one. Using our solar $T(\tau)$ relation from the convection simulations, we find a change somewhat similar to that depicted in Fig. 12, although with half the range and the solar location defining the zero-point; The cool dwarfs get larger convection zones by 0.04 of their radii and the $4.5 M_{\odot}$ HB star has its convection zone decreased by 0.018 of its radius.

Many semi-empirical solar atmosphere models do not include the Rosseland optical depth scale, but are only given on the monochromatic 5000 \AA , τ_{5000} -scale. On the other hand, opacities for stellar structure calculations only include Rosseland averages, but not the 5000 \AA opacity. When trying to combine $T(\tau_{5000})$ and κ_{Ross} in the atmosphere of a stellar structure calculation, an obvious

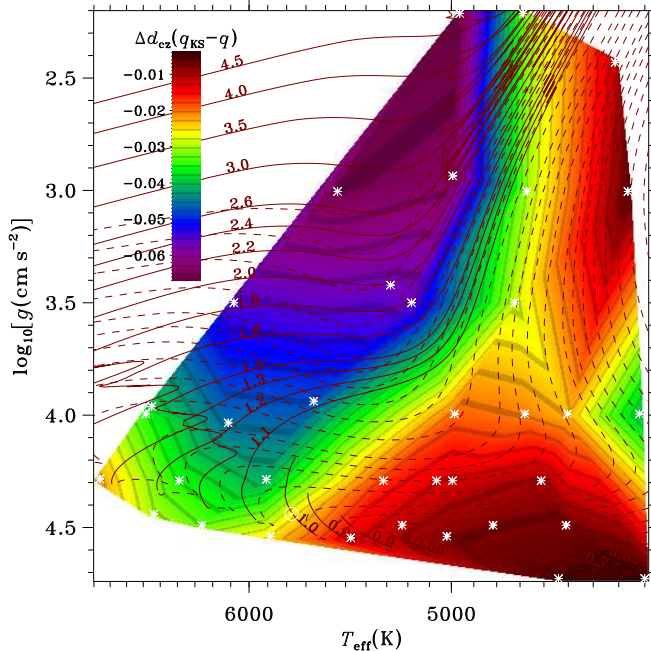


Figure 12. Envelope models employing the Krishna Swamy (1966) $T(\tau)$ relation instead of the individual ones derived from the simulations have a systematically shallower convection zone. Also compare with Fig. 8. See Fig. 1 for further explanation of the plot.

inconsistency emerges, which has been largely ignored. Fig. 13 shows to what extent this is a good approximation. It shows how the depth of convection zones of 1D envelope models changes when using $T(\tau_{5000})$ relations from the simulations together with Rosseland opacities. We see that the change is fairly small, mostly well below 1% of the stellar radius, with models more massive than the Sun having deeper convective envelopes when applying a consistent set of $T(\tau)$ relations and opacities. Our solar case has a convection zone deeper by 0.3% of R_{\odot} with the consistent combination. The one simulation with a fairly large change, 1.4% of its radius, also has the largest $\kappa_{5000}/\kappa_{\text{Ross}}$ -ratio in the photosphere. This ratio only exceeds unity in the photospheres of the stars along the low- T_{eff} border of our grid. This ratio *does* exceed unity for all the other simulations at some point higher in their atmospheres.

We recommend to use modern $T(\tau)$ relation based on modern opacities, and if possible, using those same opacities in the atmospheres of the stellar structure models. This is both to ensure consistency and in order to try to separate radiative and convective effects. This makes it possible to have the correct behaviour for stars other than the Sun, which still provides the strongest observational constraints for an α calibration.

From the above analysis, we have seen how the depth of the convective envelope depends on three parameters of the atmosphere: the mixing length, α , the $T(\tau)$ relation and the opacity. Conversely, it is also clear that an inadequate knowledge of $T(\tau)$ relation and atmospheric opacity can be absorbed into α , so that different MLT parameters can result in the same overall stellar struc-

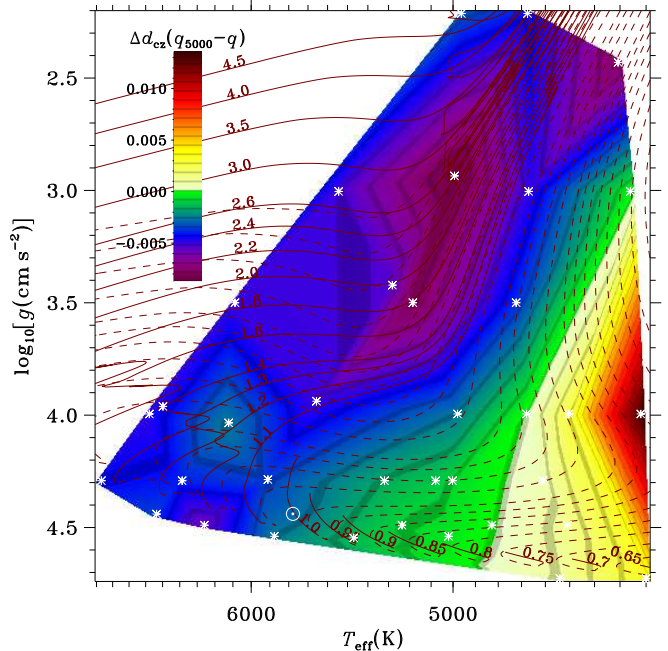


Figure 13. Envelope models employing $T(\tau)$ relations on the monochromatic τ_{5000} -scale in combination with the usual Rosseland opacities have systematically shallower convection zones, except for the coolest part of the grid where the convective envelopes deepen. Also compare with Fig. 8. See Fig. 1 for further explanation of plot.

ture (i.e., result in the deep convective envelope lying on the same adiabat). This is the most likely reason for the variation in the solar-calibrated α_{\odot} in the literature. Consistent treatment of the atmosphere will hopefully tighten the range of α_{\odot} .

7.3 Calibrating α with fixed $T(\tau)$ relation

In many cases stellar models are computed using scaled solar $T(\tau)$ relations; this includes many of the α calibrations against observations discussed below (see Sect. 8.2). We therefore performed such a calibration, based on a fit to the quiet-Sun stratification of the semi-empirical atmosphere model of Vernazza, Avrett & Loeser (1981), referred to as VAL-C. This choice of $T(\tau)$ relation is the default in, e.g., the ASTEC stellar structure code (Christensen-Dalsgaard 2008) and the closely related stellar envelope code employed here. ASTEC is also part of the Asteroseismic Modeling Portal (AMP) by Metcalfe, Creevey & Christensen-Dalsgaard (2009). AMP was used for the seismic α calibrations of Mathur et al. (2012), Bonaca et al. (2012) and Metcalfe et al. (2014). For this experiment only, we use the envelope code with its default choice of $T(\tau)$ relation.

In Fig. 14 we show the differences in α between this calibration with fixed $T(\tau)$ relation, and our full calibration with individual $T(\tau)$ relations from the simulations (Sect. 6 and Fig. 4). In both cases the calibrations are performed as outlined in Sect. 5, the only difference being the choice of $T(\tau)$ relation. We note that with the VAL-C atmosphere, α calibrates to systematically larger values

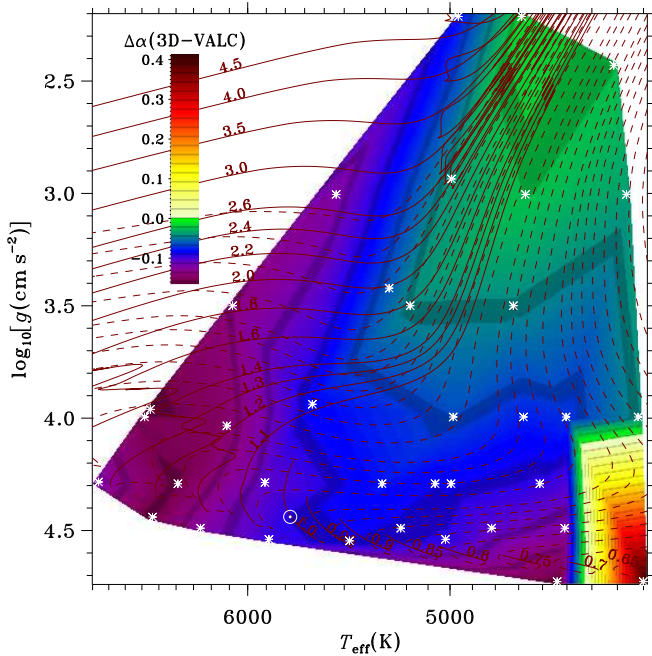


Figure 14. A calibration of MLT α based on 1D envelope models using scaled solar $T(\tau)$ relations from the semi-empirical VAL-C solar atmosphere model Vernazza, Avrett & Loeser (1981). We show the difference in α from this calibration, and the one shown in Fig. 4 based on individual $T(\tau)$ relations of the convection simulations. The singular positive value for our coolest dwarf is discussed in Sect. 7.3.

than in the full calibration, except for our coolest dwarf simulation (No. 36 of Table 1). For that case $\alpha(\text{VALC})$ is 0.41 smaller. This is a robust result. We have traced this change of sign and magnitude of α 's sensitivity to the $T(\tau)$ relation, to an extended overlap of the photosphere and the top of the convection zone in the envelope model. The convective flux increases from 3.2% to 28% of the total flux, at $\tau = 1$ between the two coolest dwarf simulations in our grid. Constructing 10 envelope models, with parameters linearly interpolated between the two calibrated models, we find a continuous, but rapid increase of the photospheric convective flux fraction towards lower T_{eff} . At $\tau = 2$ the increase is from 6.7% to 43%. The consequence is that the $T(\tau)$ relation very directly determines the adiabat of the convection zone of the coolest dwarf, whereas the warmer models have the structure effects of the $T(\tau)$ relation diminish with depth, before appreciable convection is reached. We have further attributed the outward migration of the convection zone to the effect of H_2 dissociation on ∇_{ad} , which for this cool dwarf model is suppressed from its fully ionised value of 2/5 to 0.095 centred at $\log \tau = -2.8$ and a value of 0.23 at $\tau = 1$. The outward decrease in ∇_{ad} induces a shoulder in F_{conv} , increasing in amplitude as the H_2 feature in ∇_{ad} moves inward with decreasing T_{eff} . This extension of convection into the photosphere by H_2 dissociation, was also found by Nordlund & Stein (2001).

We also see this phenomenon in our 3D simulation, with similar behaviour of ∇_{ad} and a corresponding shoulder on F_{conv} . In 3D the feature is smoothed, compared

with the 1D model, by the convective fluctuations. The effect is therefore not due to the atmospheric simplifications of 1D models; rather its physical reality is supported by our 3D simulations.

The effect of the difference in $T(\tau)$ relation is to increase the overall density of the 1D envelope by about 0.1 dex, translating into the large difference in α . For all the other cases, the resulting change in interior density is small and negative. We have not yet found the underlying reason for this difference. For our solar case, $\alpha(\text{VALC})$ is 0.09 larger than the calibration with its own 3D $T(\tau)$ relation. The difference is a minimal 0.013 for our $T_{\text{eff}} = 4962$ K giant (simulation No. 2 of Table 1) and largest for the simulations with T_{eff} around 6400 K, as well as for the next coolest dwarf (simulation No. 37 of Table 1).

7.4 Is $\partial d_{\text{cz}}/\partial \alpha$ always positive?

An analytical analysis of $\partial d_{\text{cz}}/\partial \alpha$ was carried out by Christensen-Dalsgaard (1997) (hereafter C-D97). His analysis was concerned with a highly simplified but instructive model: approximating the convective envelope with a mass-less (assuming all the stellar mass resides in the radiative interior) polytrope of index γ , which relates pressure, p , to density, ρ , through $p = K\rho^\gamma$. Further assuming hydrostatic equilibrium and a fully ionised perfect gas, he obtained the differential of the stellar radius, R , (C-D97 equation [9])

$$\partial R = -H_p \left(\frac{R}{r_{\text{cz}}} \right)^2 \partial \ln p_{\text{cz}} + \frac{R^2 d_{\text{cz}}}{r_{\text{cz}}} \left[\frac{\partial \ln K}{\gamma} + \frac{\gamma - 1}{\gamma} \partial \ln p_{\text{cz}} \right] \quad (12)$$

where r_{cz} ³ is the radius of the bottom of the convection zone and H_p is the pressure scale height at r_{cz} . Using C-D97's equation [6] we define C_1

$$C_1 \equiv -\frac{4 - \kappa_T}{(4 - \kappa_T)(\gamma - 1) - \gamma(\kappa_p + 1)} \simeq \frac{\partial \ln p_{\text{cz}}}{\partial \ln K}, \quad (13)$$

which contains the temperature and pressure derivatives of the Rosseland opacity,

$$\kappa_T \equiv \left(\frac{\partial \ln \kappa}{\partial \ln T} \right)_p, \quad \kappa_p \equiv \left(\frac{\partial \ln \kappa}{\partial \ln p} \right)_T, \quad (14)$$

at r_{cz} . With equation (13) we can eliminate the pressure, p_{cz} , in equation (12) and using C-D97's equation [15]

$$\frac{\partial \ln K}{\partial \ln \alpha} \simeq \frac{2\Delta s}{c_p} \quad (15)$$

where c_p is the specific heat at constant pressure at r_{cz} , we arrive at

$$\frac{\partial R}{\partial \ln \alpha} = \left\{ C_1 H_p \left(\frac{R}{r_{\text{cz}}} \right)^2 - \frac{R^2 d_{\text{cz}}}{r_{\text{cz}}} \left[C_1 + \frac{1 - C_1}{\gamma} \right] \right\} \frac{2\Delta s}{c_p}. \quad (16)$$

Δs is the change of specific entropy from the entropy minimum at the top of the convection zone, and down to the

³ Note that C-D97 used the symbol d_{cz} for the absolute depth of the convection zone, whereas we use it for the relative depth. Compared with his equations, all occurrences of d_{cz} are therefore multiplied by R (r_{cz} is unchanged).

adiabatic part, integrating over the peak in the superadiabatic gradient near the surface. This entropy change is positive according to the Schwarzschild criterion for convective instability, equation (1).

For the location of the bottom of the convection zone, C-D97 found

$$\frac{\partial r_{cz}}{\partial \ln \alpha} = C_1 H_p \frac{2\Delta s}{c_p}. \quad (17)$$

Combining equations (16) and (17) with $\delta(Rd_{cz}) = \delta R - \delta r_{cz}$, and

$$\delta d_{cz} = \frac{\delta(Rd_{cz})}{R} - d_{cz} \frac{\delta R}{R}, \quad (18)$$

we finally obtain

$$\frac{\partial d_{cz}}{\partial \ln \alpha} = \left\{ \frac{C_1 H_p}{r_{cz}} - C_1 - \frac{1 - C_1}{\gamma} \right\} d_{cz} \frac{2\Delta s}{c_p}. \quad (19)$$

In order for this to be positive, we therefore require the curly bracket to be positive. This can be recast into the surprisingly simple inequality

$$\frac{r_{cz}}{H_p} > \frac{4 - \kappa_T}{\kappa_p + 1} \quad \text{for } C_1 < 0, \quad (20)$$

(assuming that $4 - \kappa_T > 0$) and the opposite inequality for $C_1 > 0$.

Under which circumstances do we have $C_1 < 0$? From equation (13) we find that this is the case when

$$\gamma > \frac{4 - \kappa_T}{4 - \kappa_T - (\kappa_p + 1)}. \quad (21)$$

At the bottom of convective envelopes this is often fulfilled since κ_T is negative and of large absolute value and κ_p is positive and small, so that the right-hand side of equation (21) will not be much larger than 1. In the solar case, with $\kappa_T = -3.61$ and $\kappa_p = 0.58$ we get 1.22, which indeed is smaller than the fully ionised, ideal gas value of $\gamma = 5/3$.

The bottom of a convective envelope occurs where the radiative temperature gradient drops below the adiabatic temperature gradient [cf. equations (1) and (10)]. Assuming that the convective envelope is *not* deep enough to reach into the core (in which case the assumptions of mass-less envelope and constant luminosity would break down), the drop in ∇_{rad} will be due to a decrease in opacity. We therefore expect a large and negative κ_T . The pressure dependence of the opacity is generally much weaker than the temperature dependence, and it is in general positive. The criterion for the depth of a convective envelope to increase with α , will therefore in general be that of equation (20), which is fulfilled for all the stars considered in the present paper. In particular, for the Sun the above analysis results in $\partial d_{cz}/\partial \alpha = 0.16$. Despite the differences in the two methods; analytic versus numerical and simplified full stellar model versus detailed, but truncated envelope models, this value is close to our result, $\partial d_{cz}/\partial \alpha = 0.12$.

8 OBSERVATIONAL CONSTRAINTS

8.1 Depth of the solar convection zone

One of the simulations in our grid, No. 30, corresponds to the Sun, and we have carefully adjusted the entropy of the inflowing gas (a constant) to obtain an effective temperature of 5774 ± 15 K, in agreement with that derived from total solar irradiance (TSI) observations: $T_{\text{eff},\odot} = 5777 \pm 2.5$ K, (Willson & Hudson 1988). A recent, but contentious, reassessment by Kopp & Lean (2011) of a number of space-based, TSI measurements, find a significantly lower quiet-Sun TSI of $S_0 = (1.3608 \pm 0.0005) \times 10^6 \text{ W m}^{-2}$, corresponding to $T_{\text{eff},\odot} = 5770.35 \pm 0.15$ K. This is, however, well inside the RMS-scatter of our solar simulation. The composition of this simulation is $X = 73.70\%$ and $Z = 1.800\%$, as for the rest of the grid, and as detailed in Sect. 3. This is very close to the $X = 73.73\%$ and $Z = 1.806\%$ composition of the present day convection zone of model S (Christensen-Dalsgaard et al. 1996).

Matching this simulation to an envelope-model gives $\alpha = 1.76 \pm 0.03$, $\beta = 0.81 \pm 0.06$ and a depth of the solar convection zone, $d_{cz} = 0.2791 \pm 0.0009 R_\odot$. This is within a mere 2.5σ of the value inferred from inversion of helioseismic observations: $d_{cz} = 0.287 \pm 0.003 R_\odot$ (Christensen-Dalsgaard, Gough & Thompson 1991) and $d_{cz} = 0.287 \pm 0.001 R_\odot$ (Basu & Antia 1997). It is interesting to note that the d_{cz} that results from our calibrated α is only a little deeper than the $d_{cz} = 0.276 R_\odot$ found by, e.g., Serenelli et al. (2009), from matching L_\odot and R_\odot of models based on the Asplund et al. (2009) abundances. The uncertainties that we quote for our results are the RMS scatter resulting from performing the full fitting of $T(\tau)$ relations and envelope-matching for the individual time-steps of the relaxed and horizontally averaged simulation. No attempt at accounting for systematic effects has been carried out here.

As indicated below equation (4), there are two more parameters to standard MLT: Φ and η . These MLT-parameters and α are not linearly independent and we therefore limit ourselves to add η to our discussion, keeping $\Phi = 2$. As stated earlier, the α calibration presented here, does not reproduce the atmospheric structure of the 3D simulations, it is rather constructed to reproduce the structure inside the chosen matching point. That means the extra free parameter of MLT can be used for matching some other feature of the 3D simulations. We choose the height of the super-adiabatic peak, and the amplitude of super adiabaticity at the matching point, as two illustrative examples.

Fitting η with respect to the height of the super-adiabatic peak we get $\alpha = 1.84$, $\beta = 0.79$ and $\eta = 0.0749$, resulting in $d_{cz} = 0.2792 R_\odot$, also about 2.5σ shallower than inferred from helioseismology. The peak in the super-adiabatic gradient is increased from 0.554 in our standard calibration, to 0.695 with this new value of η .

If on the other hand we adjust the form factor, η , so as to obtain the same ∇ at the matching point, then we get $\alpha = 3.61$, $\beta = 0.50$ and $\eta = 6.41 \times 10^{-4}$, and a $d_{cz} = 0.2816 R_\odot$, 1.7σ shallower than the helioseismic

result. However, the peak of the super-adiabatic gradient becomes nonphysically large, reaching a value of 2.154, about 100 km below the photosphere. This is 3.1 times larger than what we find in the solar simulation and even more than twice as large as the super-adiabatic gradient averaged over only the upflows in the simulation.

That T , ρ and ∇ cannot be simultaneously matched at a common pressure-point (with plausible parameters), indicates that the MLT formulation converges slowly, if ever, towards the super-adiabatic gradient, $\nabla - \nabla_{\text{ad}}$, of a real convective envelope. This might be due to the neglect of kinetic-flux in the MLT formulation, as discussed in Sect. 2.

Notice that the depth of the solar convection zone, as found above, results from *ab initio* calculations, from the EOS and opacity calculations, to the RHD simulations. Apart from the defining parameters (surface gravity, entropy of the inflows at the bottom, and the composition), the adjustable parameters that enter the simulations are the resolution, the viscosity coefficients, and the size of the time step relative to the Courant time. These are tuned to resolve the thermal boundary layer at $\tau = 1$ and the convective structures, to minimize numerical diffusion while avoiding numerical noise, and to minimize the computing time against accuracy. None of these are adjusted to fit solar observations and these parameters are therefore not “adjustable parameters” in the conventional sense. In particular, no parameters have been adjusted to obtain a certain atmospheric entropy jump, or by implication, a certain mixing length, α . The close agreement with helioseismology is therefore very encouraging.

We also note that the α calibration is insensitive to the new abundances by Asplund et al. (2009), since these differ by having lower C, N and O abundances than what we employ, whereas the Fe abundance is unchanged. The latter greatly affects the solar atmosphere, but C, N and O provide little opacity here, and have little effect on the solar surface layers. The calibration is performed entirely on quantities that are minimally affected by such abundance differences, and in a region of each model with minimal sensitivity to these differences. The translation to a depth of the convective envelope, however, depends on the opacity at the bottom of the convection zone which has major contributions from oxygen (Badnell et al. 2005).

8.2 Some calibrations against stellar observations

There are several semi-empirical calibrations of the mixing length, based on stellar evolution calculations of binaries or stellar clusters, solving for a common age of the stars under the observational constraints. These cannot be compared directly with each other or with our work, since they will depend on details of the adopted convection formulation and treatment of the outer boundary condition, as discussed in Sect. 7. It is, fortunately, a widespread practice to also provide α_{\odot} of a solar model calibrated to the present radius and luminosity (Gough & Weiss 1976), and the differential behaviour with respect to the Sun should be much more robust. In the following,

we therefore compare with our results scaled to the α_{\odot} of each study, as well as with our unscaled results.

In such a semi-empirical calibration of the α Cen system, Morel et al. (2000) found $\alpha_{A,B} = (1.86^{+0.09}_{-0.06}, 1.97^{+0.13}_{-0.13})$, whereas we find values for the two components of 1.75 ± 0.03 and 1.76 ± 0.02 , respectively (No. 24 and 34 in Table 1 and Fig. 1). Yıldız (2007) found that α values of 1.64 for the primary and 1.58 for the secondary can reproduce both classic and seismic observational constraints. These are all shown in the right-hand-side of Fig. 15d. We notice that the results of Morel et al. (2000) decrease with T_{eff} , ours are both indistinguishable from the solar value, and those of Yıldız (2007) increase with T_{eff} . The latter have no error bars, but we have assigned a $\sigma_{\alpha} = 0.05$ based on the scatter in α between the models used for his analysis. The absolute values of different mixing-length calibrations are not expected to agree, since they depend on details in the modelling of the atmospheres. The differences between the two components should be more reliable, though, and we note that all three calibrations can be brought to overlap when each pair is allowed to shift vertically. Also note, however, that only the results of Morel et al. (2000) overlap with their solar-calibrated α_{\odot} (same value for those two calibrations) shown with black dotted line.

Stassun et al. (2004) performed a calibration on a pre-main-sequence (PMS) eclipsing binary in Orion, V1174 Ori. Their observations and analysis favour inefficient convection of about $\alpha = 1.0$ (compared with their $\alpha_{\odot} = 1.9$) in the pair. This is also supported by the only 0.2-0.3 dex depletion of lithium in the 1.01 M_{\odot} primary component, while the 0.73 M_{\odot} secondary displays more than 1 dex depletion. These α values do not agree with our calibration, however, where the primary should have $\alpha_A = 1.06\alpha_{\odot}$. The secondary lies 600 K outside our grid, along a steep gradient, and we attempt no extrapolation. The nearest point in our grid has $\alpha = 2.02$. Stassun et al. (2004) kept α identical for the two components, which might account for some of their problems fitting both stars to the same PMS evolution calculations.

By matching observed and model properties Fernandes et al. (1998) found that three sets of nearby visual binaries could all be described with a solar mixing length of 1.7 ± 0.3 . Within the error-bars, this is consistent with our calibration, although we would expect larger values for the cooler secondary components, as shown in Fig. 15b. Fernandes, Morel & Lebreton (2002) studied the visual binary 85 Peg and found $\alpha_A^{\text{obs}}(85 \text{ Peg}) = 1.80 \pm 0.05$ and $\alpha_B^{\text{obs}}(85 \text{ Peg}) = 2.14 \pm 0.10$, compared with their solar value of 1.9. This last result is in excellent absolute agreement with ours, $\alpha_A^{3D}(85 \text{ Peg}) = 1.76 \pm 0.02$ and $\alpha_B^{3D}(85 \text{ Peg}) = 2.05 \pm 0.03$, as shown in Fig. 15a.

Chieffi, Straniero & Salaris (1995) calibrated α against Galactic globular clusters, by either calibrating the temperatures of the red-giant branches (RGBs) or the slope of the main sequences. This latter method depends on α being constant in T_{eff} and $\log g$, from the faint end of the main sequence to 2 mags below the turn off. They divided their results into two metallicity groups, $[\text{Fe}/\text{H}] = -1.3$ and -2.3 , both with statistically insignificant differences between the main sequence and the red-giant branch, but a tentative in-

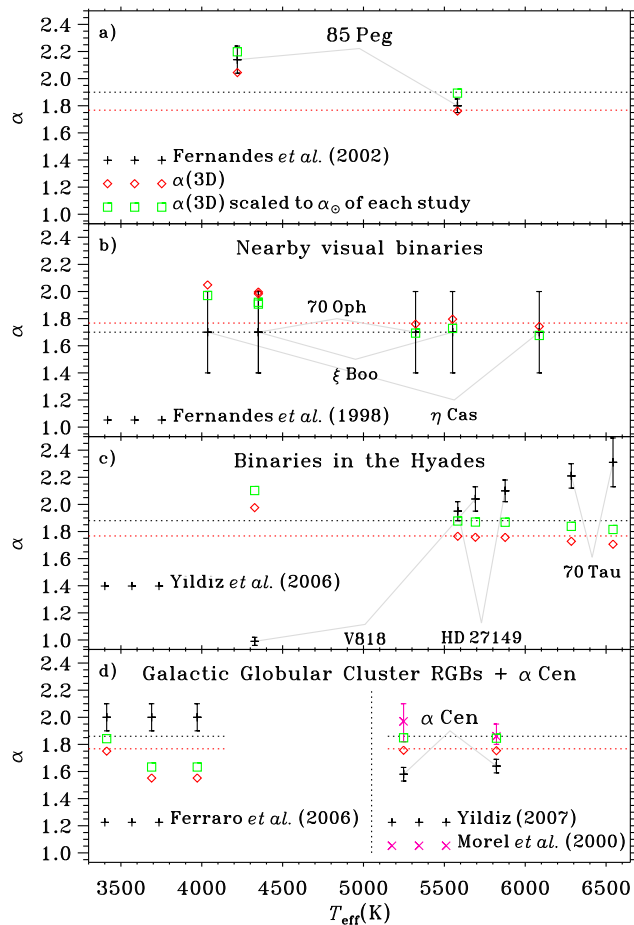


Figure 15. Comparison between our α_{MLT} calibration (red diamonds, error-bars are similar to the symbol size) and some semi-empirical calibrations from the literature (black crosses with error-bars). The respective solar calibrations of those studies are shown with horizontal black dotted lines, and the green squares show our results scaled to those solar values. The horizontal red dotted lines show our α_{\odot} . Binaries are connected with grey lines and labelled. See text for details on the six semi-empirical calibrations shown here. Our solar metallicity calibration has been extrapolated in T_{eff} to obtain the values for the metal-poor globular clusters in the left-hand side of panel d), as explained in the text.

crease with metallicity. The lack of change between the MS and the RGB, along with the location of $t \gtrsim 9$ Gyr isochrones, agrees with the triangular plateau we find in our calibration for *solar metallicity*. Their results of $\alpha_{\odot} = 2.25$, $\alpha_{\text{RGB}}([\text{Fe}/\text{H}] = -1.3) = 1.91 \pm 0.09$ and $\alpha_{\text{RGB}}([\text{Fe}/\text{H}] = -2.3) = 1.55 \pm 0.23$ is consistent with a linear increase with metallicity, assuming similar behaviour with T_{eff} and $\log g$ at all metallicities.

Fitting to observed RGBs of 28 Galactic globular clusters as function of metallicity in the range $-2.15 < [\text{Fe}/\text{H}] < -0.2$, Ferraro et al. (2006) found that the Sun and the RGB could be modelled with a common mixing length of 2.17, independent of metallicity. This followed from using the classic Anders & Grevesse (1989)-abundances with $(Z/X)_{\odot} = 0.0275$. Using instead the more modern abundances of Lodders (2003), with

$(Z/X)_{\odot} = 0.0117$, they found $\alpha_{\odot} = 1.86$ and $\alpha_{\text{RGB}} \simeq 2$, likewise independent of metallicity, as shown in Fig. 15d. This result contradicts the findings of Chieffi, Straniero & Salaris (1995) mentioned above. Our results for this case are extrapolations to both lower T_{eff} and $\log g$, so they should be interpreted with caution. This particular extrapolation almost follows the contours of $\alpha(T_{\text{eff}}, \log g)$, though, making the extrapolation less suspect. The extrapolation in metallicity is potentially a bigger issue, but the apparent lack of metallicity dependence of their results, warrants a comparison with our $[\text{Fe}/\text{H}] = 0.0$ grid.

Piau et al. (2011) studied the red (cool) edge of the RGB, based on a sample of 38 nearby Galactic disk sub-giants and giants with interferometrically determined radii. They find that the red edge, constrained by six stars, is best fitted with $\alpha = 1.68$ compared with their solar calibration of $\alpha_{\odot} = 1.98$. They also find that a single value fits the observations over a decade of luminosity, in agreement with our calibration showing RGB evolution along contours of α . Our results suggest, however, that α_{RGB} , for their mass of $0.95 M_{\odot}$, should be only 0.04 smaller than α_{\odot} . Their sample is close to solar metallicity, with the spread of the observations around the evolution tracks being accounted for by the metallicity effect on the stellar models.

Studying binaries in the Hyades, Yıldız (2006) found a mixing length that varies a factor of 2.3 over the MS mass-range of $0.77\text{--}1.36 M_{\odot}$. Our calibration suggests a factor 1.15 variation instead, and in the opposite sense (See Fig. 15c).

With further constraints from asteroseismic observations and analysis Mathur et al. (2012) found α ranging from 1.6 to 2.2 for 22 main sequence *Kepler* targets ranging from 0.8 to $1.3 M_{\odot}$. They found a possible increase of α with T_{eff} , possibly with a bump around $T_{\text{eff}} \sim 5800$ K of amplitude ~ 0.2 , but with sizable scatter. Bonaca et al. (2012) similarly found a weak increase with T_{eff} (without a bump, though) and also with $\log g$ and metallicity, $[\text{Fe}/\text{H}]$, for the main-sequence stars in their sample. Both of these results are contingent on the prescriptions for accounting for the *surface effect*: the systematic frequency shift between observations and 1D MLT models that signal differences around the upper turning point of the modes (Christensen-Dalsgaard & Thompson 1997; Kjeldsen, Bedding & Christensen-Dalsgaard 2008). The surface effect constitutes a sizable systematic effect in both analyses. Recently Metcalfe et al. (2014) analysed 42 *Kepler* targets including solar-like oscillators, F-stars and subgiants, taking special care to physically constrain the surface effect. They find α -values that agree with our calibrations, although the dependency on both T_{eff} and $\log g$ is stronger than ours. The metallicities of their sample ranges from $[\text{Fe}/\text{H}] = -0.6$ to $+0.5$ with an average and RMS-scatter of -0.06 ± 0.20 , as well as a single metal-poor star of $[\text{Fe}/\text{H}] = -1.14$. They find that α increases with $[\text{Fe}/\text{H}]$, and that the behaviour with T_{eff} and $\log g$ does not change significantly when only the solar metallicity, $|[\text{Fe}/\text{H}]| < 0.2$, sub-sample is analysed.

In general, the range of α values from our calibration is smaller than what is suggested by the various types of stellar model fitting employed above. This can be due to a number of issues, both in the modelling and in the in-

interpretations of observations. In the former category, any inadequacies or inconsistencies in the treatment of atmospheric opacities and $T(\tau)$ relations will be absorbed into the calibrated values of α . In the latter category, the translation between observations (whether photometric or spectroscopic) and T_{eff} is one of the most important. To take the temperature of a star is a non-trivial endeavour, but recent advances have been made by, e.g., Casagrande et al. (2010) and Meléndez et al. (2010) based on observations of solar twins (stars that are spectroscopically and photometrically indistinguishable from the Sun), and by Huber et al. (2012) based on asteroseismic analysis of *Kepler* and CoRoT observations, coupled with interferometric measurements of stellar radii. These calibrations of the T_{eff} -scale are being used in an absolute calibration of a range of photometric systems, based on synthetic photometry of the grid of simulations that we present here.

The mixing length of stellar atmosphere models has also been calibrated against stellar spectra, which is a profoundly different kind of calibration. Fuhrmann, Axer & Gehren (1993), van't Veer-Menneret & Mégessier (1996) and Gardiner, Kupka & Smalley (1999) all found that only a small value of $\alpha = 0.5$ can reproduce the shape of solar Balmer lines. This is half of the atmospheric mass mixing length found by Trampedach & Stein (2011), and thus does not reflect the scale of mixing. Nor does it correspond to the entropy jump in the atmosphere, which is effectively the quantity calibrated when observed global properties are fitted with evolution models. Instead it reflects the larger super-adiabatic gradient of the warm granules, which dominate the emergent spectrum, including the Balmer lines, due to their brightness (Asplund 2005; Trampedach 2010). The solar Balmer lines have been successfully modelled in NLTE, based on a 3D convection simulation (Pereira et al. 2013), and less successfully with 1D PHOENIX models (Hauschildt, Allard & Baron 1999, using $\alpha = 1.0$) and MARCS models (Gustafsson et al. 2008, using $\alpha = 1.5$).

The effects on stellar evolution models, of varying both the $T(\tau)$ relation and α according to our simulations, will be addressed in Paper III.

9 CONCLUSION

We have calibrated the MLT parameter α by matching 1D envelope models with 3D RHD simulations, and established a significant variation of α with stellar atmospheric parameters T_{eff} and g_{surf} . Our results show a triangular plateau with $\alpha \simeq 1.76$ stretching from the bottom of the red-giant branch at $\log g = 3.3$ to $T_{\text{eff}} \sim 6400\text{--}4800\text{ K}$ on the main sequence. A similar plateau was found in the calibration by LFS against 2D simulations. This plateau includes the Sun, as well as the α Cen system and their evolution so far. This suggests a common and constant α for the evolution from the main sequence of these three stars, but much of the pre-main-sequence evolution would have occurred with higher α , as shown in Fig. 4.

As stars ascend the giant branch we see that they evolve largely along contours of constant α . During this

evolutionary stage α decreases with mass, from $\alpha(M = 0.4) = 1.75$ to $\alpha(M = 4.8 M_{\odot}) = 1.56$ (simulations No. 2 to 3). The largest gradients in α occur during the evolution of low mass stars, $M < 0.8 M_{\odot}$, and for higher mass stars, $M > 1.2 M_{\odot}$, crossing the Hertzsprung gap after the turn-off from the main sequence.

Although various values of α have been considered in the modelling of stellar evolution, an α varying during the evolution of a star has, to our knowledge, not been tried yet. Results of such evolution calculations are presented in Paper III.

In Sect. 7 we investigated how changes to the radiative part of the outer boundary affect the structure of a star, using the depth of the outer convection zone as a global measure. We evaluated the linear response of the change in depth of the convection zone caused by changes in atmospheric opacity, $T(\tau)$ relation and mixing length, respectively. Our analysis in Sect. 7.1 shows that the convection zone is about equally sensitive to the three kinds of changes, and consequently different MLT parameter triplets can easily result in the same global properties of a stellar model. References to a particular mixing length are therefore less useful unless accompanied by references to the atmospheric opacity and $T(\tau)$ relation.

We also compared the effects of various commonly used assumptions about the $T(\tau)$ relation, and concluded that using the old solar $T(\tau)$ relation as given by Krishna Swamy (1966), scaled to the T_{eff} of each star, results in convection zones that are shallower by up to 7% of the radius (see Fig. 12). Using scaled versions of the $T(\tau)$ relation from the solar simulation also introduces systematic effects, causing deeper convection zones in stars cooler than the Sun and shallower ones in warmer stars. Using a 5000 \AA $T(\tau)$ relation with a Rosseland opacity has a similar but smaller effect. We recommend a consistent usage of $T(\tau)$ relations and their corresponding opacities in stellar structure and evolution calculations.

We stress that the choice of α depends on the choice of atmospheric physics, i.e., $T(\tau)$ relation and atmospheric opacity. Employing the commonly used scaled solar $T(\tau)$ relation will alter the effect of α , as shown in Sect. 7.2 and Sect. 7.3. We recommend that our calibrated α values be used with the atmospheric opacities and individual $T(\tau)$ relations from Paper I.

As ground-based and especially space-borne asteroseismology with CoRoT and *Kepler* is now providing strong constraints on the structure of stars other than the Sun, stronger demands are placed on our theoretical models. Keeping our models ahead of the asteroseismic capabilities of the next missions, TESS and PLATO, and the recently launched astrometry mission, Gaia, is a great challenge for the modelling community.

An absolute calibration of the mixing-length parameter, α , is the first step towards improving the treatment of convection in stellar structure models. A fundamentally improved formulation of convection is of course desirable, but has proven rather difficult to come by. Various attempts have been made to rectify this situation. Canuto (1992) present a formulation based on fully developed turbulence, which, however, does not account for the steep density gradient and the inherent asymmetry between up- and downflows. Lydon, Fox & Sofia (1992)

base their model on 3D hydrodynamical simulations of convection, and this is probably the most promising way forward. A number of approximations render their results less than optimal for the next generation of convection models, however.

With the connection between MLT and realistic 3D convection simulations, discussed in Sect. 2 and by Trampedach & Stein (2011), we find a properly calibrated mixing-length formulation, with the mixing length being proportional to the pressure scale height, to be the best choice for the time being.

Data Retrieval: A file with the calibrated mixing length parameters and Fortran77 routines for reading and interpolating the data can be downloaded from: <http://cdsarc.u-strasbg.fr/viz-bin/qcat?J/MNRAS/442/805> The data-file contains both the radiative Hopf functions, $q(\tau_{\text{Ross}})$, as found in Paper I, and the calibrated mixing-length parameter, α , as function of atmospheric parameters, T_{eff} and $\log g$. The URL also contains the routines necessary for setting up and interpolating in the triangulation of the irregular grid of simulations (Renka 1984). Finally, we also supply a simple user-level function to include in stellar structure codes, which does not require any knowledge of the data or the details of the triangulation.

The OPINT opacity interpolation package can be downloaded from <http://phys.au.dk/~hg62/OPINT>, together with the atmospheric opacities from our calculation (Paper I, Sect. 3.1), merged with interior OP opacities (cf. Sect. 4).

ACKNOWLEDGEMENTS

We thank the anonymous referee for helpful comments which have substantially improved the presentation. We are grateful to Werner Däppen for granting us access to the MHD-EOS code and to R. F. Kurucz for providing us with his tables of opacity distribution functions. Funding for the Stellar Astrophysics Centre is provided by The Danish National Research Foundation (Grant DNR106). The research is supported by the ASTERISK project (ASTERoseismic Investigations with SONG and *Kepler*) funded by the European Research Council (Grant agreement no.: 267864). We would like to thank the Australian Partnership for Advanced Computations (APAC) for generous amounts of computer time. RT acknowledges funding from NASA grants NNX08AI57G and NNX11AJ36G and from the Australian Research Council (grants DP 0342613 and DP 0558836) RFS acknowledges NSF grant AGS-1141921 and NASA grant and NNX12AH49G. This research has made use of NASA's Astrophysics Data System Bibliographic Services.

REFERENCES

Abbett W. P., Beaver M., Davids B., Georgobiani D., Rathbun P., Stein R. F., 1997, *ApJ*, 480, 395
Alexander D. R., Ferguson J. W., 1994, *ApJ*, 437, 879

Anders E., Grevesse N., 1989, *Geochim. Cosmochim. Acta*, 53, 197
Asida S. M., 2000, *ApJ*, 528, 896
Asplund M., 2005, *ARA&A*, 43, 481
Asplund M., Grevesse N., Sauval A. J., Scott P., 2009, *ARAA*, 47, 481
Asplund M., Ludwig H.-G., Nordlund Å., Stein R. F., 2000, *A&A*, 359, 669
Asplund M., Nordlund Å., Trampedach R., Stein R. F., 1999, *A&A*, 346, L17
Augustson K., Rast M., Trampedach R., Toomre J., 2011, *J. of Phys. Conf. Series*, 271, 012070
Augustson K. C., Brown B. P., Brun A. S., Miesch M. S., Toomre J., 2012, *ApJ*, 756, 169
Badnell N. R., Bautista M. A., Butler K., Delahaye F., Mendoza C., Palmeri P., Zeppen C. J., Seaton M. J., 2005, *MNRAS*, 360, 458
Bahcall J. N., Basu S., Pinsonneault M., Serenelli A. M., 2005, *ApJ*, 618, 1049
Baker N. H., Gough D. O., 1979, *ApJ*, 234, 232
Basu S., Antia H. M., 1995, *MNRAS*, 276, 1402
Basu S., Antia H. M., 1997, *MNRAS*, 287, 189
Belkacem K., Samadi R., Goupil M., Kupka F., 2006, *A&A*, 460, 173
Böhm-Vitense E., 1958, *Zs. f. Astroph.*, 46, 108
Bonaca A. et al., 2012, *ApJ*, 755, L12
Canuto V. M., 1992, *ApJ*, 392, 218
Canuto V. M., 2000, *A&A*, 357, 177
Canuto V. M., Mazzitelli I., 1991, *ApJ*, 370, 295
Canuto V. M., Mazzitelli I., 1992, *ApJ*, 389, 724
Casagrande L., Ramírez I., Meléndez J., Bessell M. S., Asplund M., 2010, *A&A*, 512, A54
Chan K. L., Sofia S., 1987, *Science*, 235, 465
Chan K. L., Sofia S., 1989, *ApJ*, 336, 1022
Chieffi A., Straniero O., Salaris M., 1995, *ApJ*, 445, L39
Christensen-Dalsgaard J., 1997, in *Solar Convection and Oscillations and their Relationship*, Pijpers F. P., Christensen-Dalsgaard J., Rosenthal C. S., eds., Kluwer, Dordrecht, 3
Christensen-Dalsgaard J., 2008, *ApSS*, 316, 13
Christensen-Dalsgaard J. et al., 1996, *Science*, 272, 1286
Christensen-Dalsgaard J., Frandsen S., 1983, *Sol. Phys.*, 82, 165
Christensen-Dalsgaard J., Gough D. O., Thompson M. J., 1991, *ApJ*, 378, 413
Christensen-Dalsgaard J., Pérez Hernández F., 1991, in *Lecture Notes in Physics*, Vol. 388, *Challenges to Theories of the Structure of Moderate-Mass Stars*, Gough D. O., Toomre J., eds., Springer, Berlin, 43
Christensen-Dalsgaard J., Thompson M. J., 1997, *MNRAS*, 284, 527
Collet R., Asplund M., Trampedach R., 2007, *A&A*, 469, 687
Däppen W., Mihalas D., Hummer D. G., Mihalas B. W., 1988, *ApJ*, 332, 261
Dziembowski W. A., Pamyatnykh A. A., Sienkiewicz R., 1991, *MNRAS*, 249, 602
Eggleton P. P., 1983, *MNRAS*, 204, 449
Espinosa Lara F., Rieutord M., 2011, *A&A*, 533, A43
Ferguson J. W., Heffner-Wong A., Penley J. J., Barman T. S., Alexander D. R., 2007, *ApJ*, 666, 261

- Fernandes J. M., Lebreton Y., Baglin A., Morel P., 1998, *A&A*, 338, 455
- Fernandes J. M., Morel P., Lebreton Y., 2002, *A&A*, 392, 529
- Ferraro F. R., Valenti E., Straniero O., Origlia L., 2006, *ApJ*, 642, 225
- Freytag B., Ludwig H.-G., Steffen M., 1996, *A&A*, 313, 497
- Freytag B., Steffen M., 2005, in *The A-Star Puzzle*, Zverko J., Žižňovský J., Adelman S. J., Weiss W. W., eds., Symp. No. 224, IAU, Univ. Press, Cambridge, 139
- Fuhrmann K., Axer M., Gehren T., 1993, *A&A*, 271, 451
- Gardiner R., Kupka F., Smalley B., 1999, *A&A*, 347, 876
- Georgobiani D., Stein R. F., Nordlund Å., 2003, *ApJ*, 596, 698
- Gong Z., Däppen W., Zejda L., 2001, *ApJ*, 546, 1178
- Gough D. O., 1977, *ApJ*, 214, 196
- Gough D. O., Weiss N. O., 1976, *MNRAS*, 176, 589
- Grèvesse N., Sauval A. J., 1998, *Space Sci. Rev.*, 85, 161
- Grigahcène A., Dupret M.-A., Gabriel M., Garrido R., Scudlaire R., 2005, *A&A*, 434, 1055
- Grossman S. A., 1996, *MNRAS*, 279, 305
- Gustafsson B., Edvardsson B., Eriksson K., Jørgensen U. G., Nordlund Å., Plez B., 2008, *A&A*, 486, 951
- Hauschildt P. H., Allard F., Baron E., 1999, *ApJ*, 512, 377
- Heney L., Vardya M. S., Bodenheimer P., 1965, *ApJ*, 142, 841
- Houdek G., Rogl J., 1996, *Bull. Astron. Soc. India*, 24, 317
- Huber D. et al., 2012, *ApJ*, 760, 32
- Hui-Bon-Hoa A., LeBlanc F., Hauschildt P. H., Baron E., 2002, *A&A*, 381, 197
- Hummer D. G., Mihalas D., 1988, *ApJ*, 331, 794
- Iglesias C. A., Rogers F. J., 1996, *ApJ*, 464, 943
- Kim Y.-C., Fox P. A., Sofia S., Demarque P., 1996, *ApJ*, 461, 499
- Kjeldsen H., Bedding T. R., Christensen-Dalsgaard J., 2008, *ApJ*, 683, L175
- Kopp G., Lean J. L., 2011, *Geophys. Res. Lett.*, 38, L01706
- Krishna Swamy K. S., 1966, *ApJ*, 145, 174
- Kuhfuß R., 1986, *A&A*, 160
- Kupka F., Ballot J., Muthsam H. J., 2009, *Comm. Asteroseism.*, 160, 30
- Kurucz R. L., 1992a, *Rev. Mex. Astron. Astrofis.*, 23, 45
- Kurucz R. L., 1992b, *Rev. Mex. Astron. Astrofis.*, 23, 181
- Kurucz R. L., 1992c, in *The Stellar Populations of Galaxies*, Barbuy B., Renzini A., eds., Symp. No. 149, IAU, Springer, Dordrecht, 225
- Lesaffre P., Podsiadlowski P., Tout C. A., 2005, *MNRAS*, 356, 131
- Lodders K., 2003, *ApJ*, 591, 1220
- Lucy L. B., 1967, *Zeit. f. Astroph.*, 65, 89
- Ludwig H.-G., Freytag B., Steffen M., 1999, *A&A*, 346, 111
- Ludwig H.-G., Nordlund Å., 2000, in *Stellar Astrophysics: Proceedings of the Pacific Rim Conference, Hong Kong, 1999*, Kluwer, Dordrecht, 37
- Lydon T. J., Fox P. A., Sofia S., 1992, *ApJ*, 397, 701
- Mathur S. et al., 2012, *ApJ*, 749, 152
- McQuillan A., Mazeh T., Aigrain S., 2013, *ApJ*, 775, L11
- McQuillan A., Mazeh T., Aigrain S., 2014, *ApJS*, 211, 24
- Meléndez J., Schuster W. J., Silva J. S., Ramírez I., Casagrande L., Coelho P., 2010, *A&A*, 522, A98
- Metcalfe T. S., Creevey O. L., Christensen-Dalsgaard J., 2009, *ApJ*, 699, 373
- Metcalfe T. S. et al., 2014, *ApJS*, arXiv:1402.3614, (accepted)
- Miesch M. S., Brun A. S., Toomre J., 2006, *ApJ*, 641, 618
- Militzer B., Hubbard W. B., 2013, *ApJ*, 774, 148
- Morel P., Provost J., Lebreton Y., Thévenin F., Berthomieu G., 2000, *A&A*, 363, 675
- Nayfonov A., Däppen W., Hummer D. G., Mihalas D., 1999, *ApJ*, 526, 451
- Nielsen M. B., Gizon L., Schunker H., Karoff C., 2013, *A&A*, 557, L10
- Nordlund Å., 1974, *A&A*, 32, 407
- Nordlund Å., 1976, *A&A*, 50, 23
- Nordlund Å., 1982, *A&A*, 107, 1
- Nordlund Å., Dravins D., 1990, *A&A*, 228, 155
- Nordlund Å., Stein R. F., 1990, *Comput. Phys. Commun.*, 59, 119
- Nordlund Å., Stein R. F., 1991, in *Stellar Atmospheres: Beyond Classical Models*, et al. L. C., ed., Kluwer, Dordrecht, 263
- Nordlund Å., Stein R. F., 1997, in *Solar Convection and Oscillations and their Relationship*, Pijpers F. P., Christensen-Dalsgaard J., Rosenthal C. S., eds., Kluwer, Dordrecht, 79
- Nordlund Å., Stein R. F., 2000, in *The Impact of Large-Scale Surveys on Pulsating Star Research*, Szabados L., Kurtz D. W., eds., ASP Conf. Ser. 203, IAU Coll. No. 176, ASP, San Francisco, 362
- Nordlund Å., Stein R. F., 2001, *ApJ*, 546, 576
- Paxton B., Bildsten L., Dotter A., Herwig F., Lesaffre P., Timmes F., 2011, *ApJS*, 192, 3
- Pereira T. M. D., Asplund M., Collet R., Thaler I., Trampedach R., Leenaarts J., 2013, *A&A*, 554, A118
- Piau L., Kervella P., Dib S., Hauschildt P. H., 2011, *A&A*, 526, A100
- Rempel M. D., 2004, *ApJ*, 607, 1046
- Renka R. J., 1984, *ACM Trans. on Math. Softw.*, 10, 440
- Renzini A., 1987, *A&A*, 188, 49
- Richard O., Dziembowski W. A., Sienkiewicz R., Goode P. R., 1998, in *Structure and Dynamics of the Interior of the Sun and Sun-like Stars*, Korzennik S. G., ed., SOHO 6/GONG 98 Workshop, ESA, Noordwijk, 517
- Rieutord M., Zahn J.-P., 1995, *A&A*, 296, 127
- Rogers F. J., Iglesias C. A., 1992, *ApJS*, 79, 507
- Rogers F. J., Nayfonov A., 2002, *ApJ*, 576, 1064
- Rosenthal C. S., Christensen-Dalsgaard J., Nordlund Å., Stein R. F., Trampedach R., 1999, *A&A*, 351, 689
- Samadi R. et al., 2013, *A&A*, 559, A40

- Samadi R., Georgobiani D., Trampedach R., Goupil M., Stein R. F., Nordlund Å., 2007, *A&A*, 463, 297
- Saumon D., Chabrier G., Horn H. M. V., 1995, *ApJS*, 99, 713
- Seaton M. J., ed., 1995, *The Opacity Project*, Vol. 1. Institute of Physics Publishing
- Serenelli A. M., Basu S., Ferguson J. W., Asplund M., 2009, *ApJ*, 705, L123
- Shaviv G., Salpeter E. E., 1973, *ApJ*, 184, 191
- Spiegel E. A., 1963, *ApJ*, 138, 216
- Stassun K. G., Mathieu R. D., Vaz L. P. R., Stroud N., Vrba F. J., 2004, *ApJS*, 151, 357
- Stein R. F., Benson D., Georgobiani D., Nordlund Å., 2007, in *Convection in Astrophysics*, Kupka F., Roxburgh I., Chan K. L., eds., Symp. No. 239, IAU, Cambridge University Press, 331
- Stein R. F., Georgobiani D., Trampedach R., Ludwig H.-G., Nordlund Å., 2005, in *XXVth General Assembly*, Engvold O., ed., *Highlights of Astronomy* No. 13, IAU, ASP, San Francisco, 411
- Stein R. F., Nordlund Å., 1989, *ApJ*, 342, L95
- Stein R. F., Nordlund Å., 1998, *ApJ*, 499, 914
- Stein R. F., Nordlund Å., 2001, *ApJ*, 546, 585
- Stein R. F., Nordlund Å., 2003, in *Stellar atmosphere modeling*, Hubeny I., Mihalas D., Werner K., eds., *ASP Conf. Ser. No. 288*, 519
- Stellingwerf R. F., 1976, *ApJ*, 206, 543
- Tanner J. D., Basu S., Pierre D., 2014, *ApJ*, 785, L13
- Trampedach R., 2005, in *The A-Star Puzzle*, Zverko J., Žižňovský J., Adelman S. J., Weiss W. W., eds., Symp. No. 224, IAU, Univ. Press, Cambridge, 155
- Trampedach R., 2010, *Ap&SS*, 328, 213
- Trampedach R., Asplund M., Collet R., Nordlund Å., Stein R. F., 2013, *ApJ*, 769, 18
- Trampedach R., Christensen-Dalsgaard J., Nordlund Å., Asplund M., Stein R. F., 2014, *MNRAS*, 442, 805
- Trampedach R., Christensen-Dalsgaard J., Nordlund Å., Stein R. F., 1997, in *Solar Convection and Oscillations and their Relationship*, Pijpers F. P., Christensen-Dalsgaard J., Rosenthal C. S., eds., Kluwer, Dordrecht, 73
- Trampedach R., Stein R. F., 2011, *ApJ*, 731, 78
- Turcotte S., Richer J., Michaud G., Iglesias C. A., Rogers F. J., 1998, *ApJ*, 504, 539
- Ulrich R. K., 1970, *Ap&SS*, 9, 80
- Ulrich R. K., 1976, *ApJ*, 207, 564
- van't Veer-Menneret C., Mégessier C., 1996, *A&A*, 309, 879
- Vernazza J. E., Avrett E. H., Loeser R., 1981, *ApJS*, 45, 635
- von Zeipel H., 1924, *MNRAS*, 84, 684
- Vorontsov S. V., Baturin V. A., Pamyatnykh A. A., 1991, *Nature*, 349, 49
- Walkowicz L. M., Basri G. S., 2013, *MNRAS*, 436, 1883
- Willson R. C., Hudson H. S., 1988, *Nature*, 332, 810
- Yıldız M., 2006, *MNRAS*, 368, 1941
- Yıldız M., 2007, *MNRAS*, 374, 1264

This paper has been typeset from a \TeX / \LaTeX file prepared by the author.